Journal of Natural Gas Science and Engineering 105 (2022) 104721

Contents lists available at ScienceDirect

Journal of Natural Gas Science and Engineering

journal homepage: www.elsevier.com/locate/jngse

Adsorbents selection for the enrichment of low-grade methane coal mine emissions by temperature and pressure swing adsorption technologies

David Ursueguía, Eva Díaz, Salvador Ordóñez *

Catalysis, Reactors and Control Research Group (CRC). Department of Chemical and Environmental Engineering, Faculty of Chemistry, University of Oviedo, 33006, Spain

ARTICLE INFO

Keywords:
Ventilation air methane
Fixed-bed adsorption
Process simulation
Temperature swing adsorption
Pressure swing adsorption
Coal mine emissions

ABSTRACT

This work evaluates the feasibility of common adsorbents (carbonaceous materials, zeolites and metal-organic frameworks) for the adsorption and further methane upgrading of the ventilation air methane (VAM) emissions from underground coal mining (0.57% CH_4). Concentration was achieved by adsorption through two different operational procedures based on fixed bed configurations: temperature swing adsorption (TSA) and pressure swing adsorption (PSA). All the combinations have been simulated using a rigorous mathematical model implemented in a commercial simulation package. The main purpose is to evaluate the performance of the different combinations of adsorption technique and adsorbent material, as well as establishing a valid mathematical model able to test a wide range of materials. The comparison has been fulfilled with an economic evaluation of the different combinations. Results show that carbonaceous materials provide the highest concentration factors ($C/C_0 = 5$), with low total methane recoveries (30%) and the lowest cost per kmol of methane recovered (1.5 €/kmol). MOFs can retain substantial amounts of methane, but with lower CH_4/N_2 selectivities than carbonaceous materials and lower methane concentration factors ($C/C_0 = 2.6$). For this type of materials, a high recovery of methane is achieved, but at expense of the highest costs (80 €/kmol). Finally, zeolitic materials present the lowest methane concentration factor ($C/C_0 = 2$), with intermediate both methane recoveries (58%) and costs (25 €/kmol). Concerning the adsorption technique, TSA has shown higher final methane concentrations for carbonaceous materials and some MOFs, whereas PSA overperforms for zeolitic materials. In addition, TSA is cheaper in all cases than PSA processes. On the other hand, PSA allows higher total methane recoveries and adsorption capacities for all materials, highlighting the high dependence on adsorption pressure, especially in carbonaceous materials (PSA/TSA = 18.3, in the case of Maxsorb).

1. Introduction

In the frame of the European Green Deal, the European Commission proposed in September 2020 raising the 2030 greenhouse gas (GHG) emission reduction target, including emissions and removals, to at least 55% compared to 1990 (climate and energy framework, 2030). Among the considered sources, the energy sector accounts for around 75% of the total GHG emissions (Damassa, 2014). Therefore, minimizing the emission of these streams is a requirement for climate neutrality. In this way, methane recovery is a major challenge from two points of view: the reduction of global warming (methane global warming potential is twenty-one times greater than carbon dioxide (Howarth, 2014)) and obtaining an efficient and clean fuel source, as well as a basic raw material for synthesizing several chemical products (Kilkis et al., 2020). Most methane emissions have an anthropogenic origin, being classified into biogenic (55%) (Pandey and Harpalani, 2019), thermogenic (22%) and pyrogenic (13%), among others (Schoell, 1988; Pieprzyk and Hilje, 2018). Biogenic methane is generated via microbial methanogenesis, under an anaerobic atmosphere at given ambient conditions, e.g., the methane generated from underground coal or rice crops (Park and Liang, 2016). Thermogenic methane is related to the methane generated by geological processes and contained in fossil fuels such as coal, oil, and natural gas (Thiagarajan et al., 2020). Finally, pyrogenic methane is related to biomass or biofuels incomplete combustions (Sapart et al., 2012). Most of these methane emissions are hardly recoverable, such as those from agriculture, livestock, or transport (Khokhar and Park, 2017). The same occurs for fugitive methane emissions from oil and natural gas industries, which consist mainly of gas leaks in conductions, venting, deliberate combustions or even in leaks in the final product

* Corresponding author.
E-mail address: sordonez@uniovi.es (S. Ordóñez).

https://doi.org/10.1016/j.jngse.2022.104721
Received 4 May 2022; Received in revised form 23 June 2022; Accepted 14 July 2022
Available online 19 July 2022
1875-5100/© 2022 The Authors. Published by Elsevier B.V. This is an open access article under the CC BY-NC-ND license (http://creativecommons.org/licenses/by-nc-nd/4.0/).

Abbreviations

VAM	Ventilation air methane
TSA	Temperature swing adsorption
PSA	Pressure swing adsorption
MOFs	Metal-organic frameworks
GHG	Greenhouse gases
CBM	Coal bed methane
AMM	Abandoned mine methane
CHP	Combined heat and power
VSA	Vacuum swing adsorption
TVSA	Temperature and vacuum swing adsorption
VPSA	Vacuum and pressure swing adsorption
VTVSA	Vacuum and temperature swing adsorption
USD1	Unparameterized supervised discretization
LDF	Linear driving force

SYMBOLS

u_0	Surface velocity (m/s)
d_p	Particle diameter (m)
C_b	Vessel fixed cost (€)
S	Vessel external surface area (m^2)
t	Time (s)
C	Methane concentration in gas phase (mol/m^3)
W	Methane concentration in solid phase (mol/kg)
Q	Energy required in heat exchanger (W)
C_p	Specific heat (J/mol·K)
$\dot{n}$	Molar flow (mol/s)
A	Heat exchanger surface area (m^2)
T_2-T_1	Heat exchanger temperature increment (K)
U	Overall heat-transfer coefficient ($W/m^2 \cdot K$)
ΔT_{ln}	Logarithmic mean temperature difference (K)
W_c	Compression power (W)
γ	Adiabatic expansion coefficient
V_1	Initial volume (m^3)
V_2	Final volume (m^3)
P_1	Initial pressure (Pa)
P_2	Final pressure (Pa)
D_e	Axial dispersion coefficient (m^2/s)
ε_b	Bed void fraction
z	Axial position in the fixed bed (m)
$\overline{q}$	Adsorbate concentration equilibrium in gas phase (mol/m^3)
q_e	Adsorption equilibrium (mol/m^3)
q_e^*	Adsorbate concentration equilibrium in solid phase (mol/kg)
K_L	Overall mass transfer coefficient (s^{-1})
r_p	Particle radius (m)
k_f	External film mass transport coefficient (m/s)
ε_p	Particle porosity
D_p	Diffusivity in macropores (m^2/s)
r_c	Crystallite radius (m)
D_i	Micropores diffusivity term (m^2/s)
C_0	Initial adsorption concentration (mol/m^3)
q_0	Initial adsorption capacity (mol/m^3_{solid})
dP	Pressure gradient (Pa)
μ_g	Gas viscosity (Pa·s)
ρ_g	Gas density (kg/m^3)
ρ_b	Bed density (kg/m^3)
D_m	Molecular diffusivity (m^2/s)
T	Temperature (K)
P	Pressure (Pa)
M_A	Molar mass (mol/kg)
V_A	Molar volume (mol/m^3)
h_s	Heat transfer coefficient ($W/m^2 \cdot K$)
Nu	Nusselt number
k_g	Thermal gas conductivity (W/m·K)
Pr	Prandtl number
a_p	Adsorbent surface-to-volume ratio (m^{-1})
q_m	Langmuir isotherm constant (mol/kg)
b	Langmuir exponential factor (m^3/mol)
L	Fixed bed length (m)
D	Fixed bed diameter (m)
Y_{CH4}	Methane molar fraction
C/C_0	Methane concentration factor

storage or transport (Brandt et al., 2014). Therefore, in these cases, it is recommended to minimize emissions at the source and, if it is not possible, to implement a control operation to meet regulation standards (Klein et al., 2018).

On the other hand, there are easily recoverable methane emissions using already available equipment in the facility, such as existing ducts, ventilation points and vertical wells: underground coal mining emissions. There are three types of mining emissions: coal bed methane (CBM), abandoned mine methane (AMM) and ventilation air methane (VAM). CBM comes directly from coal seams in mining, its methane content is high (around 30%), and it supposes about 30% of all the methane emitted in the exploitations (Ju et al., 2016). Its extraction process involves drilling hundreds of wells with extensive infrastructural support facilities. From this source, the United States currently produce 7% of its natural gas (Kumar, 2018). AMM refers to released methane once the mining activity stops, for up to 20 years after the closure (Kholod et al., 2020; Duda and Krzemien, 2018). Recovered methane concentrations typically range from 15 to 90%, with negligible oxygen concentrations (UNECE, 2019). Electricity generation or combined heat and power (CHP) production (Denysenko et al., 2018) are the main uses of these streams. Finally, VAM is a very diluted methane stream (0.1–1% CH_4) (Warmuzinski, 2008), which is obtained from ventilation systems designed to keep methane concentration in working galleries below the flammability limit (2% CH_4). Although their methane concentrations are very low, their huge flowrates become these emissions into the largest GHG emissions in the coal mining activity (Yang et al., 2022). In addition, the efficient use of these streams is not straightforward, due to their low methane content, so they are usually emitted directly into the atmosphere or burned with very low energetic efficiency (Yang et al., 2018). In general terms, concentrated streams (CBM and AMM) are used directly for energy production (Karacan et al., 2011), whereas VAM requires a previous concentration step for main uses. In fact, an efficient VAM recovery would mean a great decrease in methane emissions, in addition to generate a resource for energy obtaining or chemical synthesis. For example, it was demonstrated that a previous concentration process would allow obtaining adequate streams for working on gas turbines (>1% CH_4) (Ursueguía et al., 2021a).

Furthermore, add to methane and air, high relative humidity, and carbon dioxide traces (around 0.1% CO_2) are also found. Hence, the methane purification process involves the methane gas separation from the air species, water, and carbon dioxide (Ursueguía et al., 2021b). The most common and easy to scale-up processes for performing gas separations at high scales are swing adsorption methods. Among them, temperature swing adsorption (TSA) and pressure swing adsorption (PSA) are the most used (Vogtenhuber et al., 2018; Li et al., 2013), which consist of cyclic variations in temperature or pressure of the fixed bed, respectively, alternating operation conditions between two or more available beds. In recent times, different authors have reported

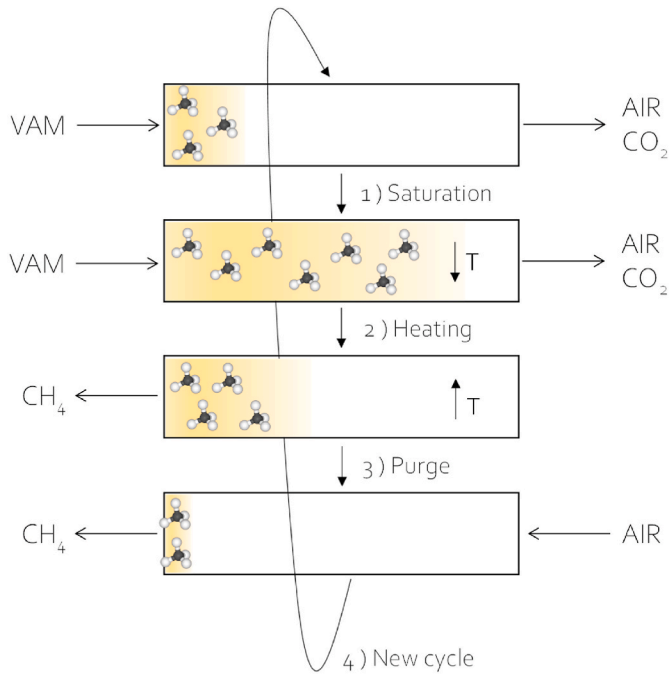

Fig. 1. TSA typical stages distribution for a VAM concentration process. The orange gradient indicates the advance of the methane adsorption front in the fixed bed.

promising results using these techniques. For example, Karimi et al. (Karimi and Fatemi, 2021) have doubled the initial methane concentration (10–20%) through a PSA process with Norit R1 activated carbon as adsorbent. On the other hand, Wang et al. (2021) have compiled several interesting results obtained through two different techniques: using TSA, the methane concentration was increased from 5 to 20% with more than 99% methane recovery, using silicalite as adsorbent; by VPSA, the methane concentration was improved from 5 to 12.6%, with a

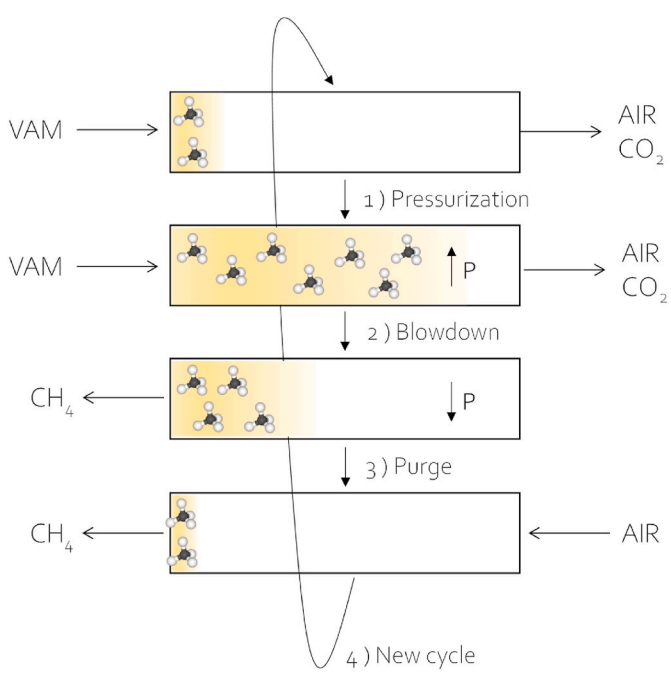

Fig. 2. PSA typical stages distribution for a VAM concentration process. The orange gradient indicates the advance of the methane adsorption front in the fixed bed.

methane recovery of 81.9%, using a carbon molecular sieve (CMS) as adsorbent. Finally, Pawlaczyk-Kurek et al. (Yang et al., 2022) have presented examples of different methane-enriching processes by swing adsorption techniques (PSA, VSA, TVSA, VPSA, VTVSA) with different adsorbents (coconut shell, activated carbon and honeycomb monolithic carbon). These results seem promising for almost all cases, especially in case of VTVSA, even already checked at pilot plant level. Even so, the simplicity of TSA and PSA processes makes them an adequate starting point to know the validity of a material for the desired separation (Vogtenhuber et al., 2018; Karimi and Fatemi, 2021; Yang et al., 2020; Bahamon and Vega, 2016; Maring and Webley, 2013; Dantas et al., 2011; Qu et al., 2020). It should be also noted that these techniques can be combined for obtaining optimal results.

Although methane concentration from nitrogen-rich streams is reported in the literature, these studies do not start from concentrations as low as those present in VAM streams (0.1–1%). The scope of these articles is studying in detail a technique and adsorbent lacking the comparison between techniques (PSA and TSA) and adsorbents. Thus, it is difficult to state with the currently available information what configuration and what kind adsorbents is better for this purpose. This fact is even more critical if the presence of spectator species (as carbon dioxide) is considered.

This work tries to fill this gap, presenting a systematic comparison of technologies and materials for accomplishing the purpose of significantly increase methane concentration in VAM emissions. For accomplishing this purpose, the $CH_4/N_2/CO_2$ separation performance from VAM streams was systematically evaluated by both PSA and TSA processes with nine different adsorbents, representative of the three main families (carbonaceous materials, zeolites, and MOFs). A rigorous mathematical model (validated at lab-scale in previous works (Ursueguía et al., 2020a)) was proposed for simulating both techniques, solving the corresponding differential equations by Aspen Adsorption software, which was also used for the estimation of the associated costs to each combination. This procedure will allow to determine the best configuration for the separation, in addition to assess the key properties of the material governing its performance for both processes.

2. Methodology

2.1. TSA and PSA features

The fixed bed design and the distribution of the operation times have been performed based on the same criteria presented in a previous work (Ursueguía et al., 2021a), in which a complete description of the typical layout of these processes has been developed. In this work, two different operation ways were considered: TSA and PSA. In a common fixed bed adsorption process, two or more fixed beds are in series in the same stage, thus maintaining one of them always practically fresh in an alternating mode (Couper et al., 2005). Here, only the performance of one of these fixed beds will be considered, focusing more on the comparison of materials and techniques.

In case of TSA (Fig. 1), the adsorption and desorption steps are accomplished by varying the temperature of the fixed bed. First, an adsorption stage, in which the temperature is as low as possible, and the components of the inlet mixture are selectively adsorbed depending on their affinity to the adsorbent material. In this case, the adsorption temperature is fixed by the Langmuir isotherm constants of the adsorbents, presented in a later section. Consecutively, at the desorption stage, a hot rinsing stream is introduced in counterflow direction to promote desorption, obtaining a concentrated stream in the most strongly adsorbed components. This rinsing stream is one of the optimizable parameters in the process since it is within the limits that meet the typical surface velocity interval in a fixed bed (0.2–0.5 m/s).

In this case, the same flowrate as in the adsorption process is considered to simplify the study. This approach was followed in the literature for comparing technologies and materials (Ben-Mansour and

Qasem, 2018). In the same way than adsorption, desorption temperature is fixed by the temperature of the adsorption isotherm constants selected for each case. In fact, the maximum operation temperature depends on the material stability and the process cost. Even so, considering the material and economic viability of the process, and parametric studies, such as Chen et al. (2021), it is desirable not to exceed 383 K for desorption. Finally, the cooling stage, which consists of cooling down the bed to return to the initial conditions for starting another new cycle. Generally, the most expensive stage is related to the heating of the streams, so it should be imperatively considered in the economic balance of each operation. The required energy (Q) for the desorption step is calculated assuming a heat exchange (Eq. (1)) with constant specific heat (C_p) value for air (29.17 J/mol·K), which is the cleaning gas, and the calculated molar flow ($\dot{n}$). Once the required energy is known, it is possible to design the tubular heat exchangers for the process, commonly used in processes with gases at low pressure inside the tubes. The cost is directly related to the surface area (A) of the exchanger (Equipment costs, 2003), calculated by Eq. (2), whereas the temperature increment ($T_2 - T_1$) is obtained from adsorption isotherm data reported for each material. In addition, the value of the overall heat-transfer coefficient (U) is considered as 20 W/m^2·K (Perry and Green, 1997), whereas the logarithmic mean temperature differences (ΔT_{ln}) is obtained assuming a heat exchanger where the hot fluid is steam at 373 K.

$$Q = \dot{n} \cdot C_p \cdot (T_2 - T_1) \tag{1}$$

$$Q = U \cdot A \cdot \Delta T_{ln} \tag{2}$$

In case of PSA (Fig. 2), the concentration step is carried out by decreasing the pressure of the fixed bed. The sequence consists of a first high-pressure adsorption stage, in which the pressure is highly variable and depends on the application of the gas to be treated: for example, Canevesi et al. (2019) have applied pressures between 3 and 10 bar for upgrading biogas, whereas Luberti et al. (Luberti and Ahn, 2022) have applied pressures up to 65 bar for hydrogen purification.

Afterwards, a pressure reduction step causes the desorption of the previously adsorbed components, obtaining a stream concentrated in the strongest adsorbed components (Vilardi et al., 2020). In addition, some intermediate steps can be added to optimize the systems, such as equalizations, either product-end or feed-end, to change the fixed bed pressure through connections between different beds working at the same time but in different stages of the process (Yavary et al., 2015). These steps are very brief, their duration being negligible in comparison to the total cycle time (Kim et al., 2015). Finally, the regeneration step, needed when several mixture compounds are strongly retained, even at low pressures. At this last step, a rinsing gas, generally air at low pressure, is introduced for removing these compounds. In PSA, the pressurization is the most expensive stage, so it must be considered in the economic balance. In that way, it is supposed an adiabatic compression. The required power (W_c) is calculated through Eq. (3), where is known the adiabatic expansion coefficient ($\gamma = 1.4$, for air), the initial volume (V_1), and initial and final desired gas pressure (P_1 and P_2, respectively). Additionally, the centrifugal-motor compressor cost can be –calculated from the total flow treated and the required power (Equipment costs, 2003).

$$W_c = \frac{P_1 V_1 - P_2 V_2}{1 - \gamma} \tag{3}$$

Regarding to the fixed bed, the design variables have been selected based on a common operating criterion (Ursueguía et al., 2021a). Thus, the usual surface velocity (u_0) of gases in a fixed bed is between 0.2 and 0.5 m/s, the adsorbent particle size (d_p) between 0.5 and 10 mm, and the maximum possible dimensions of the fixed bed, 14 and 3.5 m of length and diameter, respectively (Equipment costs, 2003). Also, the length of the fixed bed must be, at least, three times greater than the bed diameter (Wilkins et al., 2020). The use efficiency of the fixed bed increases with the length of the bed, since the unused part becomes a smaller portion of the total bed (Gabelman, 2017), but also increases the fixed bed costs and the total pressure drop. In fact, the fixed-bed devices present a fixed bed cost, which depends only on the size of the container: $C_b = 2310 \cdot S^{0.778}$, where C_b (€) is the total cost and S (m^2) the area of the external surface of the container (Costs reports and guidance for, 2018). Furthermore, the diameter selection must consider the exothermic nature of the process, avoiding large increases in temperature, so a high surface-to-volume ratio is desirable (Perego and Peratello, 1999).

Table 1
Initial and boundary conditions used to solve the balance differential equations.

Condition	Boundary limit
$t = 0$	$C = 0$
	$W = 0$
	$\overline{q} = 0$
$z = 0$	$(C - C_{in}) = \frac{\varepsilon_b \cdot D_e}{u_0}\left(\frac{\partial C}{\partial z}\right)$
	$\left(\frac{\partial W}{\partial z}\right) = 0$
$z = L$	$\left(\frac{\partial C}{\partial z}\right) = 0$
	$\left(\frac{\partial W}{\partial z}\right) = 0$

2.2. Mathematical model

TSA and PSA processes in a fixed bed were simulated using Aspen Adsorption software. All the combinations between adsorbent materials and adsorption techniques were simulated through a dynamic heterogeneous one-dimensional model, also accounting for axial dispersion and axial pressure gradients. For the sake of simplicity, the following assumptions were considered:

- Isothermal conditions in the adsorption step, due to the low methane and nitrogen adsorption heats (around 20 kJ/mol), which are practically constant with the total uptake (Niu et al., 2019), and the low carbon dioxide concentrations in VAM streams.
- Negligible both radial dispersion and changes in axial flow velocity, due to the limited adsorption capacities and the low methane and carbon dioxide concentrations (Ortiz et al., 2019).
- Adsorbent particles are spherical and homogeneous in size and density.
- Uniform bed void ratio for each material.

Following the previous assumptions, Eq. (4) and Eq. (5) describe the general model of a fixed-bed adsorption for the gas and solid phases, respectively. This model considers a gas transport over an axial bed, and it includes accumulation, convection, dispersion, and interphase mass transfer terms. The discretization method used to solve the equations is USD1, with 100 nodes along the axial direction. The solution shows the variation of methane concentration with time (t) in the gas (C) and solid (W) phases, respectively. The second term in the gas phase balance considers the axial dispersion (D_e) in the process, whereas the third term, convective transport, depends on the surface velocity (u_0) and on the bed void fraction (ε_b). The initial and boundary conditions used to solve the differential equations are presented in Table 1.

$$\frac{\partial C}{\partial t} - D_e \frac{\partial^2 C}{\partial z^2} + \frac{u_0}{\varepsilon_b}\frac{\partial C}{\partial z} = -\frac{(1-\varepsilon_b)}{\varepsilon_b}\frac{\partial \overline{q}}{\partial t} \tag{4}$$

$$\frac{\partial W}{\partial t} = -\frac{\partial \overline{q}}{\partial t} \tag{5}$$

The last term in Eq. (4) and Eq. (5), interphase mass transfer, has been modelled assuming the existence of a linear driving force (LDF). This assumption relates linearly the mass transport and the adsorption

Table 2
Main features of the considered materials (activated carbons, dark grey; zeolites, white; and MOFs, light grey) (Al-Naddaf et al., 2018; Du et al., 2019; Gao et al., 2012; Han et al., 2002; Hartmann and Fischer, 2012; Jadhav et al., 2007; Ursueguía et al., 2020b; Wu et al., 2005).

Material	Particle size (mm)	Packing density (g/cm^3)	Bed void space (-)	S_{BET} (m^2/g)	Pore volume (cm^3/g)	Cost (€/kg)	References
Norit R1	1	0.44	0.36	1450	0.47	0.25	[65, 66]
BPL	1.3	0.45	0.49	1150	0.43	0.62	[65, 67]
Maxsorb	1.15	0.32	0.25	3250	1.79	0.6	[65, 68]
β-zeolite	3	0.6	0.4	664	0.3	5.1	[69, 70]
Zeolite 13X	1.6	1.13	0.54	615	0.34	1.8	[71, 72]
Zeolite 5A	2.7	0.73	0.32	689	0.35	1.7	[73, 74]
MIL-101(Cr)	1.5	0.43	0.4	4100	1.9	8.2	[75, 76]
MOF-508	4.6	0.39	0.74	743	-	8.2	[77, 78]
Basolite C300	2	0.22	0.62	1467	1.24	8.2	[79, 80]

equilibrium (q_e), calculated through the adsorption isotherms of each material. This model has been used in many gas-solid adsorption cases with good accuracy to experimental results (Rupa et al., 2021). Therefore, Eq. (6) can model the mass transfer kinetics, where q_e* (mol/kg) is the adsorbate concentration at equilibrium, and K_L (s^{-1}) is the overall mass transfer coefficient, accounting for transport resistances in the external film, macropores and micropores of each adsorbent. It was obtained from reported experimental data of methane and nitrogen diffusion on each of the considered families of materials (Chaemwinyoo et al., 2022; Xu et al., 2015; Jensen et al., 2012). It can be also expressed as shown in Eq. (7), in which the first term of the equation is related to the transport resistance in the external film of the particle. It depends on the particle radius (r_p) and the external film mass transport coefficient (k_f). The second term is related to the mass transport in the macropores of the adsorbent, and it depends on the particle radius, the particle porosity (ε_p) and the diffusivity in macropores (D_p). Finally, the last term is related to the diffusivity in the micropores, and it depends on the crystallite radius (r_c) and the micropores diffusivity term (D_i). Depending on the features of each adsorbent, some terms of resistance could be negligible, as in the case of very microporous materials, which present much higher values of the last resistance term (Zhu et al., 2020).

$$\frac{\partial \overline{q}}{\partial t} = K_L\left(q_e^* - \overline{q}\right) \tag{6}$$

$$\frac{1}{K_L} = \frac{r_p \cdot q_0}{3 \cdot k_f \cdot C_0} + \frac{r_p^2 \cdot q_0}{15 \cdot \varepsilon_p \cdot D_p \cdot C_0} + \frac{r_c^2}{15 \cdot D_i} \tag{7}$$

In addition, momentum balance is calculated through Ergun equation (Eq. (8)), which relates surface velocity to pressure gradient (∂P), and it depends on the physical properties of the gas (μ_g, ρ_g) and of the solid bed (ρ_b). Once convective transport is assumed, the value of the axial dispersion coefficient (D_e) is estimated from the values of the calculated molecular diffusivities (D_m) for each case (Sabouni et al., 2013).

$$\frac{\partial P}{\partial z} = \frac{150\mu_g(1-\varepsilon_b)^2}{d_p^2 \cdot \varepsilon_b^3} u_0 + \frac{1.75 \cdot \rho_g \cdot (1-\varepsilon_b)}{d_p \cdot \varepsilon_b^3} u_0^2 \tag{8}$$

The kinetic model assumption is linear lumped resistance with fixed molecular diffusivities (D_m), calculated through Fuller-Schettler-Gridding correlation (Eq. (9)), which depends on temperature (T), pressure (P), molar mass (M_A, M_B) and molar volume (V_A, V_B) of each component of the stream. Finally, there are not chemical reactions considered in the process.

$$D_m = \frac{0.001 \cdot T^{1.75} \cdot \left(\frac{1}{M_A} + \frac{1}{M_B}\right)}{P \cdot \left(V_A^{1/3} + V_B^{1/3}\right)^2} \tag{9}$$

In addition, in case of TSA, methane desorption occurs by a drag gas at increased temperature flowing through the fixed bed. Hence, the energy balance to the gas and solid phases (Eq. (10) and Eq. (11), respectively) should be considered. The velocity at which thermal equilibrium is reached depends on the heat transfer coefficient (h_s), calculated using correlation for fixed beds based on Nusselt ($Nu = h_s \cdot d_p / k_g$) and Prandtl ($Pr = C_{p,g} \cdot \mu_g / k_g$) dimensionless numbers (Qu et al., 2020). The adsorbent surface-to-volume ratio (a_p) is also calculated for each case. The specific heat capacity of the solid (C_{ps}) is studied in several works for carbonaceous materials (Querejeta et al., 2019), with values between 0.8 and 1.2 J/g·K. Further, guided by the previous assumptions, no variation of the temperature in the solid due to the heat of adsorption is considered since the concentration of the adsorbate is low in the inlet streams. The energy balances are useful for the estimation of the time required for cooling the material after desorption in TSA processes, as it is not considered instantaneous.

Table 3
Suitable materials for gas adsorption processes with its Langmuir isotherm constants at different temperatures.

Material	Temperature (K)	CH_4		CO_2		N_2		References
		q_m (mol/kg)	b (m^3/mol)	q_m (mol/kg)	b (m^3/mol)	q_m (mol/kg)	b (m^3/mol)	
Norit R1 Extra	298	0.0381	0.0062	0.0754	0.0067	0.0095	0.0019	(Himeno et al., 2005; Dreisbach et al., 1999)
	323	0.0222	0.0040	0.0412	0.0042	0.0057	0.0013	
BPL	298	0.0260	0.0056	0.0809	0.0101	0.0034	0.0468	(Himeno et al., 2005; Delgado et al., 2014; Sircar et al., 1996; McEwen et al., 2013)
	323	0.0159	0.0041	0.0637	0.0071	0.0023	0.033	
Maxsorb	298	0.0315	0.0021	0.0595	0.0017	0.0266	0.0042	(Himeno et al., 2005; Sheikh et al., 1996; Gómez et al., 2015)
	323	0.0186	0.0013	0.0374	0.0014	0.0166	0.0028	
β-zeolite	298	0.0137	0.0164	0.1299	0.0556	0.0059	0.0216	(Li and Tezel, 2007; Xu et al., 2009)
	323	0.0136	0.0163	0.1298	0.0556	0.0059	0.0216	
Zeolite 13X	298	0.0150	0.0001	2.8301	0.4579	0.0095	0.0066	Cavenati et al. (2004)
	323	0.0075	0.0053	0.8584	0.2282	0.0042	0.0005	
Zeolite 5A	303	0.0208	0.0214	3.9841	1.2537	0.0076	0.0056	(Liu et al., 2011; Bakhtyari and Mofarahi, 2014)
	323	0.0071	0.0135	1.1250	0.3937	0.0038	0.0065	
MIL-101 (Cr)	288	0.0159	0.0229	0.2711	0.1176	0.0056	0.0011	Munusamy et al. (2012)
	313	0.0055	0.0122	0.1040	0.0467	0.0023	0.0102	
MOF-508	303	0.0347	0.0202	0.0555	0.0029	0.0468	0.0318	Bastin et al. (2008)
	323	0.0315	0.0183	0.0349	0.0007	0.0406	0.0301	
Basolite C300	298	0.0281	0.0036	0.1662	0.0186	0.0073	0.0009	(Teo et al., 2017; Kloutse et al., 2018; Nobar and Farooq, 2012)
	323	0.0068	0.0036	0.0559	0.0058	0.0026	0.0059	

$$\frac{\partial T_g}{\partial t} = -u_0\frac{\partial T_g}{\partial z} + h_s\frac{a_p}{C_{pg}\rho_g}\left(T_s - T_g\right) \tag{10}$$

$$\frac{\partial T_s}{\partial t} = h_s\frac{a_p}{C_{ps}\rho_b}\left(T_g - T_s\right) \tag{11}$$

From this model, previously validated with experimental data (Ursueguía et al., 2020a) under similar conditions and for three different adsorbent materials, in combination with adsorbent features and inlet flow properties, both the breakthrough and desorption curves, and the maximum methane concentration obtained at the outlet can be determined.

2.3. Adsorbent selection and adsorption isotherm parameters

Adsorbents typically used in gas adsorption and separation processes can be grouped in three main families: carbonaceous materials, zeolites, and MOFs. The activated carbons are the most representative of the first group (Zheng et al., 2019; Peredo-Mancilla et al., 2019), with large specific surface areas, high pore volumes and good yields in gas adsorption processes, in addition to being cheap. In case of zeolites, the adsorption and separation process are usually characterized by steric effects, depending on pore and molecular sizes (Gholipour and Mofarahi, 2016; Li and Tezel, 2007), and generally are more expensive than activated carbons. Finally, MOFs have been extensively studied in recent times due to its interesting morphological and surface properties, such as its elevated specific surface area and total pore volume (Ghazvini et al., 2021). At this time, most of the MOFs are synthesized exclusively at laboratory or small scales, so it is not possible to obtain a price comparable to the other materials. However, Neves et al. (2021) have calculated the costs associated to an ideal MOF large-scale production, setting 8.2 €/kg in the most favourable situation, which is considered in this work. The total associated cost depends on the dimensions of the fixed bed, which are directly related to the total inlet flow and the correspondent surface velocity. The selected adsorbent materials for the process are compiled in Table 2, in addition to some of its most important features.

On the other hand, the adsorption isotherm parameters, supposing Langmuir isotherm (Eq. (12)), are included in Table 3. This isotherm model has shown to fit the experimental data in practically all the partial pressure range, so it is adequate to use it in adsorption, with low partial pressures, and in desorption, when the methane concentration can reach higher values. In fact, it is one of the most used isotherms in gas adsorption available works (Cavenati et al., 2004; Brea et al., 2017). As additional advantages, it allows modelling the adsorption behaviour of the adsorbent in presence of two or more simultaneous potential adsorbates (Rainone et al., 2021), add to be applied in some fixed bed adsorption simulations to obtain the corresponding breakthrough curves (Xiu and Li, 2000).

$$q_e = \frac{q_m bC}{1 + bC} \tag{12}$$

2.4. Properties of the considered stream and comparison parameters

Each mining exploitation can present very different flowrates and concentration values in its emissions, the properties of these streams being also variable with time. In addition to methane, nitrogen and carbon dioxide, the considered streams may also contain other compounds, such as water, oxygen, and particulate matter, which could be harmful for the adsorption operation and subsequent processes. Water can be strongly adsorbed over hydrophilic adsorbents and cause structural damages in certain materials, such as MOFs (Schoenecker et al., 2012), thus it should be removed previously to the adsorption stage (Ryckebosch et al., 2011). Concerning the oxygen, with a behaviour as adsorbate similar to nitrogen (Qadir et al., 2021), it is in lower concentrations, and it is not usually considered. For example, Bae et al. (2014) considered the methane/nitrogen separation to be the most important, both in PSA and TSA processes for methane purification. Finally, the presence of solid particles could significantly reduce the adsorption available surface area of the adsorbent, in addition to be adhered on machinery, reducing thus the life cycle, and modifying the properties of commodities (Su and Agnew, 2006). To avoid its presence, Cheng et al. (2017) have compiled a great variety of techniques that could be suitable for that purpose before the adsorption process, so solid particles are not considered in the problem streams. Therefore, the streams are considered purified before the adsorption process (negligible content of solid particles and humidity), so only methane, air (nitrogen) and carbon dioxide are considered at the simulation input. VAM stream features have been selected according to the values presented in the registers of different European mining exploitations, partners of the METHENERGY + European Research Project. The flowrates of these streams can be large, up to 200 m^3/s, with low methane concentrations. In this case, a flowrate of 4.4 m^3/s, with an inlet composition of 0.57% CH_4, 0.1% CO_2, 99.3% air is considered as case study (Ursueguía et al., 2021a).

For all this, the main comparison parameters among the results of the different combinations are: 1) adsorption capacity (mol/kg), calculated

Table 4
Simulation parameters for TSA and PSA for the three carbonaceous materials considered.

TSA (P = 1 bar)									
Material	$\dot{n}$ (mol/s)	L (m)	D (m)	ε_b	ρ_b (kg/m^3)	d_p (mm)	$1/K_L$ (s)	D_m (m^2/s) (ads/des)	T (K) (ads/des)
Norit R1	60	10	2.5	0.36	440	1	0.0030	$2.1\cdot10^{-5}/2.4\cdot10^{-5}$	298/323
BPL	60	10	2.5	0.49	450	1.3	0.0018	$2.1\cdot10^{-5}/2.4\cdot10^{-5}$	298/323
Maxsorb	60	10	2.5	0.25	320	1.15	0.0023	$2.1\cdot10^{-5}/2.4\cdot10^{-5}$	298/323
PSA (T = 298 K)									
Material	$\dot{n}$ (mol/s)	L (m)	D (m)	ε_b	ρ_b (kg/m^3)	d_p (mm)	$1/K_L$ (s)	D_m (m^2/s) (ads/des)	P (bar) (ads/des)
Norit R1	60	10	2.5	0.36	440	1	0.0030	$7\cdot10^{-6}/2.1\cdot10^{-5}$	1/3
BPL	60	10	2.5	0.49	450	1.3	0.0018	$7\cdot10^{-6}/2.1\cdot10^{-5}$	1/3
Maxsorb	60	10	2.5	0.25	320	1.15	0.0023	$7\cdot10^{-6}/2.1\cdot10^{-5}$	1/3

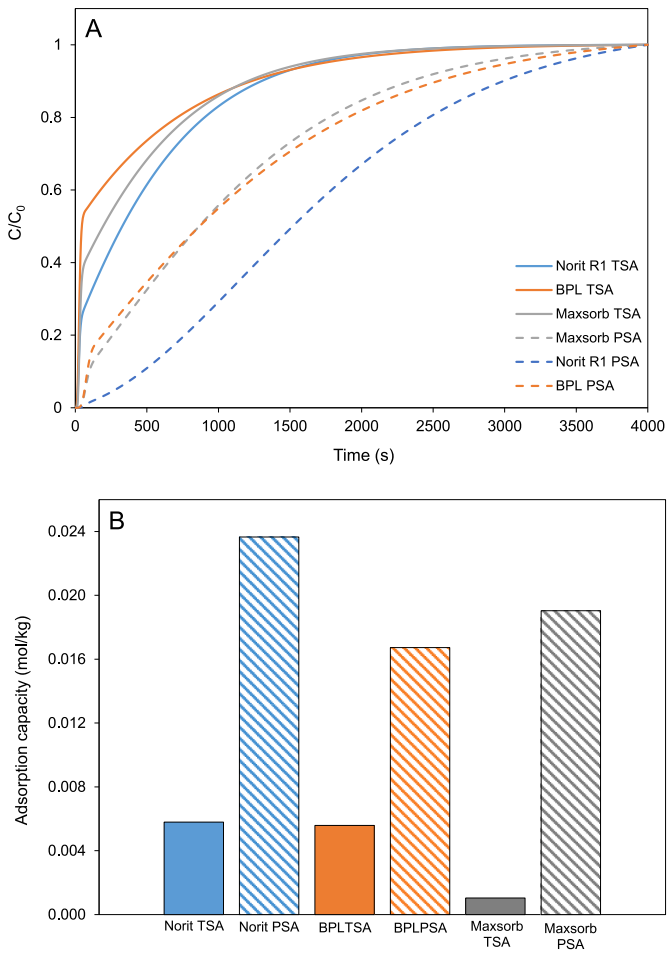

Fig. 3. Methane breakthrough curves (A) and methane adsorption capacity (B) for the carbonaceous materials studied. TSA processes performed at 298 K and 1 bar, whereas PSA processes at 298 K and 3 bar.

through the area integration of the breakthrough curve for each scenario, for a given flow rate and feed methane concentration; 2) saturation time (s), considered as the first time at which the C/C_0 in the breakthrough curve reaches a value of 1, i.e., when the material is totally saturated in the adsorbate compounds; 3) methane recovery (%), calculated as the ratio of the methane recovered by adsorption, estimated from the adsorption capacity and the quantity of adsorbent material, and the total amount of methane introduced, calculated from the inlet flow and the inlet concentration of methane; and, 4) total cost, estimated from the individual cost of every device and resource used in the process (heaters, compressors, adsorbent material, energy, etc.).

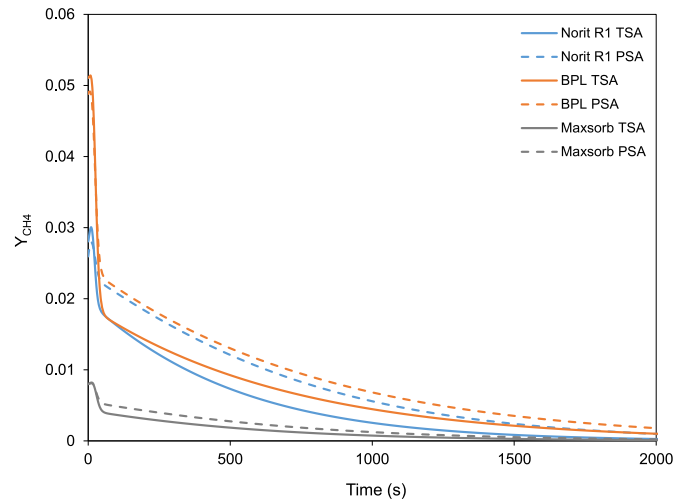

Fig. 4. Methane molar fraction in desorption curves for the carbonaceous materials studied. TSA processes simulated at 323 K and 1 bar, whereas PSA processes simulated at 298 K and 1 bar.

3. Results and discussion

Following typical fixed bed design considerations, three identical fixed beds, with dimensions of 10 m of length and 2.5 m of diameter, would be required to treat a total inlet molar rate of 60 mol/s in each one, 180 mol/s total. Two different adsorption techniques are considered: TSA and PSA. The design begins with the selection of the surface velocity, 0.3 m/s, which is an intermediate surface velocity for a fixed bed adsorption process. Desorption flowrate remains as in adsorption stage, in order to keep constant the recommended surface velocity in each fixed bed. The following sections present the design and results obtained for the three most common families of adsorbents and the two adsorption techniques considered, as well as a subsequent performance and economic comparison between all the results obtained.

3.1. Carbonaceous materials

Carbonaceous materials are some of the most used materials in gas adsorption processes, especially activated carbons, which present good values of porosity, specific surface area and adsorption capacity of different gases. The performance of three common activated carbons for the methane recovery process has been studied: Norit R1, BPL and Maxsorb. These three materials present a large contribution of micropores in their porous structure, which influences the adsorption capacity and mechanism, and hence, the predominant resistance of the process (Himeno et al., 2005). Therefore, the last term of Eq. (7), $r_c^2/15\cdot D_i$, is the prevailing in this case, considering the role of micropores. Table 4 compiles the required parameters for the three considered carbonaceous materials and the simulation conditions in each case. Mass transport

Table 5
Methane recovery values for each process with carbonaceous materials.

Material	Process	CH_4 recovery (%)
Norit R1	TSA	9.2
	PSA	37.4
BPL	TSA	9.1
	PSA	27.1
Maxsorb	TSA	1.2
	PSA	21.9

coefficients (K_L) are obtained from the adsorption experiments reported by Xu et al. (2015) on microporous carbonaceous adsorbents, these values being like those published by Golden et al. (Golden and Kumar, 1993) for different low-concentrated gases on activated carbon. The simulation is carried out in the Aspen Adsorption simulation software. Fig. 3A presents a comparison of the methane breakthrough curves, both by TSA and PSA techniques, as well as the total methane adsorption capacities for each case (Fig. 3B).

In case of Norit R1 and BPL, the adsorption capacity follows the same trend as the specific surface area, increasing the difference with pressure. Maxsorb activated carbon can be considered as an exception, since the adsorption capacity in the TSA process is very low in comparison with the other adsorbents despite having larger specific surface area and pore volume. It is demonstrated the high influence of pressure, with a methane adsorption capacity ratio between PSA and TSA of 18.3. On the other hand, Fig. 4 presents the methane concentration step at the desorption stage by both TSA and PSA. As seen, the low CH_4/N_2 selectivity, obtained from the Langmuir isotherm constants, in case of Maxsorb avoids obtaining high methane concentration values, in addition to reduce the methane adsorption capacity in favour to nitrogen at low adsorption pressures. The shape of desorption graphs is similar to the obtained by Xu et al. (Yang, 2003) in case of air separation.

High concentrations were observed for Norit R1 and BPL activated carbon, both over 1%, the necessary minimum concentration for operating a gas turbine (Ursueguía et al., 2021a). A maximum concentration of 5.1% is obtained for BPL by TSA, which constitutes an enrichment of 88.9% from the inlet stream. On the other hand, Norit R1 carbon achieves a maximum concentration of 3%, which constitutes an enrichment of 81.1%. Norit R1 and BPL present high CH_4/N_2 selectivities (5 and 4.1, respectively), obtained from the Langmuir adsorption isotherms (Eq. (12)). In addition, in case of BPL, its high affinity for carbon dioxide induces a final maximum molar concentration of 2.6% CO_2, whereas it is only 1% for Norit R1, values obtained from the simulation. Thus, it is pointed out the convenience of TSA processes to maximize the methane concentration at the outlet, in agreement with works that recommend TSA in streams with concentrations of the interesting compound lower than 2% (Xu et al., 2018; Ghoshal and Manjare, 2002). Table 5 summarizes the total recovery of methane for each case, obtained from saturation at 4000 s. The higher adsorption capacities for PSA processes lead to higher total methane recoveries. Therefore, in terms of performance, the lowest methane concentration at the outlet is obtained by PSA, but the total methane recovered is higher than in TSA. Then, a compromise must be reached depending on the final application of the obtained stream. Concerning cycles, it is possible to elucidate the required time to complete each stage of the processes. In case of TSA, a complete cycle takes 4.1 h (adsorption stage, 4000 s; heating, 4500 s; desorption, 2000 s; back to initial conditions, 4000 s), therefore, 1952 cycles/year can be reached, considering 8000 working hours.

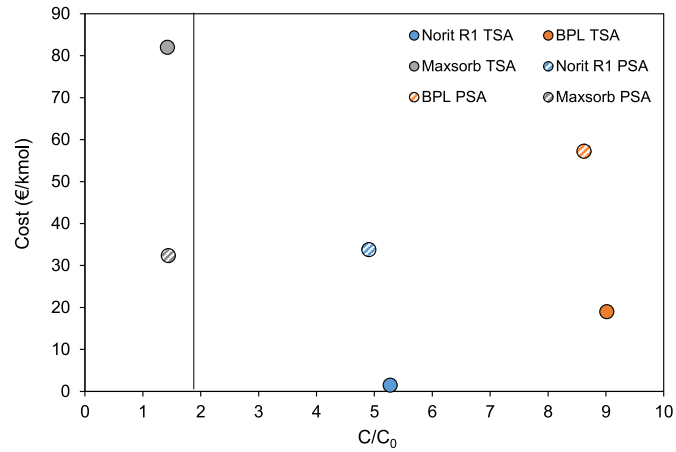

Fig. 5. Relation for all the carbonaceous materials between cost per kmol of methane recovered and the concentration times from the initial methane concentration (C_0 = 0.57%). Vertical black line points out the minimum concentration factor necessary to use the obtained stream as feed in a gas turbine (1% CH_4).

These carbonaceous materials have been proposed for VAM concentration, Bae et al., 2014, 2020 have used carbon fibre composites for the enrichment of 0.54% CH_4 VAM streams through a combination of PSA and TSA (6% CH_4) and through a two-stage combination of vacuum and temperature (20% CH_4). Although their results are better than the reported in our work, they were obtained combining both technologies, with subsequent technical complexity and larger operation costs (not evaluated by the authors). In addition, Ouyang et al. (2013) have used coconut shell VPSA to obtain 1.13% CH_4 from 0.42% CH_4, with a methane recovery of around 88%.

The costs associated with methane enrichment are evaluated supposing a flowrate of 4.4 m^3/s for desorption, the same as for adsorption. Desorption cycles are considered finished at outlet methane molar fractions (Y_{CH4}) of $5.7 \cdot 10^{-4}$ and the assumed energy cost is 0.07 €/kW·h (Ursueguía et al., 2021a). Thereby, the associated costs for each material and adsorption technique are calculated for one year (8000 working hours), average period considered for adsorbent replacement (Table 6). It is observed that the total cost per year is in all cases lower for TSA processes, due to the lower energy requirements associated to the heating process than to pressurization ones. The initial investment corresponds to vessels and exchanger for TSA; and vessels and compressor for PSA. On the other hand, annual costs correspond to adsorbent and heating for TSA, whereas in the case of PSA, they correspond to the pressurization step. Differences in cost between both techniques are high in all cases, reaching even 71% in case of Norit R1.

In addition to the costs, potential earnings should also be considered in the final economic profitability estimation. For this, all the methane recovered in each case is supposed to be burned to obtain energy. Simplifying, a complete combustion of each stream is considered, assuming a calorific potential of pure methane of 0.8 MJ/mol (NIST's Standard Reference Database Number, 1843). The cost of the energy is supposed the same (0.07 €/kW·h), and the final result is the difference

Table 6
Costs associated to the main stages in TSA and PSA processes (Couper et al., 2005).

Material	Adsorbent (k€)	Vessels (k€)	Heating[a] (k€)	Exchanger[a] (k€)	Pressurization[b] (k€)	Compressor[b] (k€)
Norit R1	16.5	206.5	32.8	15.2	582.5	128.8
BPL	41.9	206.5	33.2	21.5	567.9	128.8
Maxsorb	28.4	206.5	21.0	11.4	406.3	128.8

[a] Used in TSA processes.
[b] Used in PSA processes.

Table 7
Simulation parameters for TSA and PSA for the three zeolitic materials considered.

TSA (P = 1 bar)									
Material	$\dot{n}$ (mol/s)	L (m)	D (m)	ε_b	ρ_b (kg/m^3)	d_p (mm)	$1/K_L$ (s)	D_m (m^2/s) (ads/des)	T (K) (ads/des)
β-zeolite	60	10	2.5	0.40	600	3	0.326	$2.1\cdot10^{-5}/2.4\cdot10^{-5}$	298/323
Zeolite 13X	60	10	2.5	0.54	1130	1.6	0.029	$2.1\cdot10^{-5}/2.4\cdot10^{-5}$	298/323
Zeolite 5A	60	10	2.5	0.32	730	2.7	0.018	$2.16\cdot10^{-5}/2.4\cdot10^{-5}$	303/323
PSA (T = 298 K and 303 K for zeolite 5A)									
Material	$\dot{n}$ (mol/s)	L (m)	D (m)	ε_b	ρ_b (kg/m^3)	d_p (mm)	$1/K_L$ (s)	D_m (m^2/s) (ads/des)	P (bar) (ads/des)
β-zeolite	60	10	2.5	0.40	600	3	0.326	$7\cdot10^{-6}/2.1\cdot10^{-5}$	1/3
Zeolite 13X	60	10	2.5	0.54	1130	1.6	0.029	$7\cdot10^{-6}/2.1\cdot10^{-5}$	1/3
Zeolite 5A	60	10	2.5	0.32	730	2.7	0.018	$7.2\cdot10^{-6}/2.16\cdot10^{-5}$	1/3

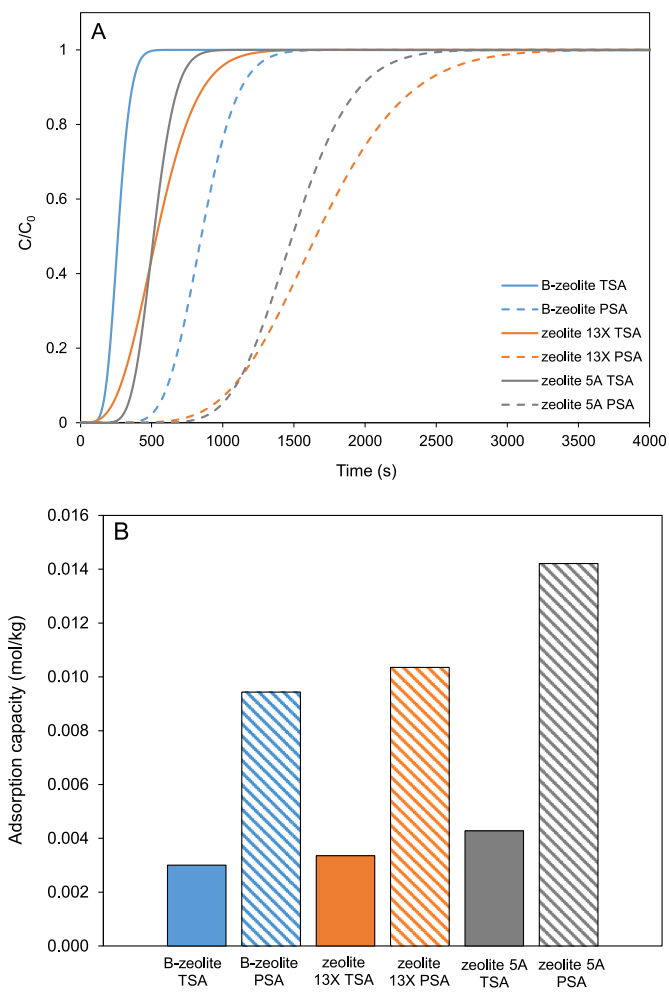

Fig. 6. Methane breakthrough curves (A) and methane adsorption capacity (B) for the zeolitic materials considered. TSA processes were performed at 298 K and 1 bar, except 303 K for zeolite 5A, whereas PSA processes were performed at 298 K and 3 bar, except 303 K for zeolite 5A.

between the costs associated to one cycle and the energetic profit obtained from the methane recovered in the same cycle. The vessels, compressors and heat exchangers costs should be only considered as initial investments and not as annual costs. As shown in Fig. 5, the process is not economically profitable in any case. The black line in the graph points out the minimum concentration factor (C/C_0) necessary for being able to use the recovered stream as feed in a gas turbine (1% CH_4). Below the 1%, it is Maxsorb activated carbon, the material with the lowest selectivity CH_4/N_2 (2.7) and the lowest methane adsorption capacity. Above 1% are both Norit R1 and BPL activated carbons, for

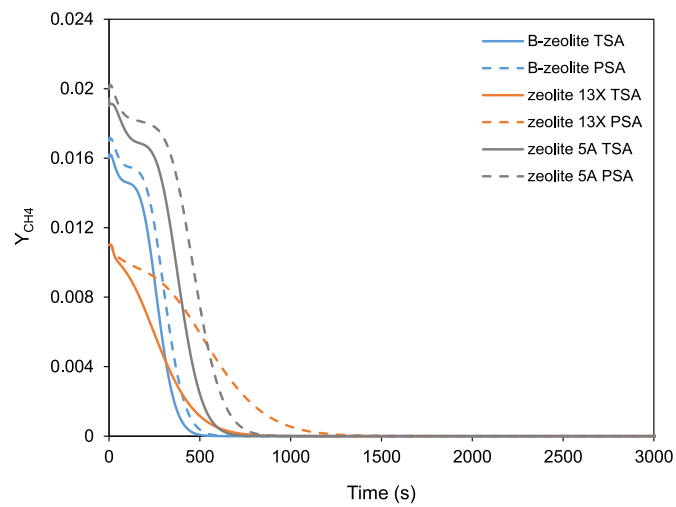

Fig. 7. Methane desorption curves for the zeolitic materials considered. TSA processes performed at 323 K, 1 bar, whereas PSA processes performed at 298 K, 1 bar.

which the PSA processes are clearly more expensive than TSA ones. In fact, Norit R1 material with the TSA process (1.47 €/kmol recovered) is near to have a null cost (0 €/kmol), which means that the annual cost of the operation would be zero.

3.2. Zeolitic materials

Zeolitic materials are very used in gas adsorption processes. Despite not presenting so good values of porosity and specific surface area like carbonaceous materials, the separation based on steric effects make them suitable materials for this purpose. In this case, three zeolitic materials were studied: β-zeolite, zeolite 13X and zeolite 5A. In case of adsorption processes with β-zeolite, the micropores influence is much higher than that of mesopores, with $1/K_L$ values of 0.326 s in case of nitrogen (Li and Tezel, 2007). Zeolite 5A is a similar case, with larger pores (Silvestre-Albero et al., 2001), and with commercial crystals generally very small and practically with no diffusional limitations, as Silva et al. (2015) have demonstrated. On the other hand, adsorption on zeolite 13X is mainly governed by diffusion both in micropores and mesopores. Therefore, mass transfer coefficient values depend on both last terms of Eq. (7), dependent on diffusion in micro and macropores, obtained from Cavenati et al. (2006) experiments. Thus, the mathematical model equation used for the modelling is different in case of zeolite 13X, which should maintain microporous and mesoporous resistance terms. Table 7 compiles the simulation parameters of the three zeolitic materials considered in the Aspen Adsorption simulation software and simulation results are presented in Fig. 6. Fig. 6A presents a comparison of the methane breakthrough curves obtained for the studied materials, both by TSA and PSA, as well as the total methane

Table 8
Methane recovery values for each process with zeolites.

Material	Process	CH_4 recovery (%)
β-zeolite	TSA	44.39
	PSA	51.36
Zeolite 13X	TSA	37.87
	PSA	53.43
Zeolite 5A	TSA	50.27
	PSA	58.07

adsorption capacities (Fig. 6B).

In this case, the total adsorption capacity is lower than for carbonaceous materials, being zeolite 5A which presents the higher adsorption capacity among these materials, attributed to the high specific surface area and total pore volume (1.79 cm^3/g). The methane adsorption capacity ratio (PSA/TSA) is 3.14, 3.08 and 3.32, respectively, for β-zeolite, zeolite 13X and zeolite 5A, being the differences between materials less significant in this parameter, in contrast to carbonaceous materials. Likewise, the effect of pressure is lower in this case. Fig. 7 presents the methane concentration values at the desorption stage by both TSA and PSA.

In this case, all the materials and techniques can provide the desired 1% of methane at the outlet. A maximum concentration of 1.9% is obtained by zeolite 5A by TSA, which constitutes an enrichment of 70% from the inlet stream, whereas β-zeolite achieves a maximum concentration of 1.6% by TSA, which constitutes an enrichment of 64.3% from the inlet stream. Opposite to carbonaceous materials, the maximum concentration obtained in each case is higher in PSA processes, staying also linger times at higher concentrations. In addition, final concentrations obtained are lower than for carbonaceous materials, as well as the CH_4/N_2 selectivities: 2.76, 1.94 and 1.87, respectively, for β-zeolite, zeolite 13X and zeolite 5A. Further, β-zeolite presents high affinity to carbon dioxide, with a final concentration of 2.7% CO_2. Table 8 shows the total recovery of methane for each case, although the saturation time depends on both the adsorbent and the technique, Fig. 6. The higher adsorption capacities in case of PSA processes lead to higher total methane recoveries. In addition, the higher material densities than in case of carbonaceous materials provoke the recovery percentages to be higher in case of zeolites.

The costs associated with methane enrichment are evaluated supposing a flowrate of 4.4 m^3/s for desorption, the same as for adsorption. The calculation procedure and the assumptions are the same than in case of carbonaceous materials, and the results are presented in Table 9.

It is observed that the annual total cost is in all cases lower for TSA processes, as well as in case of carbonaceous materials. Differences in cost between both techniques are lower than in case of carbonaceous materials, reaching 44.4% as maximum in case of zeolite 5A. Profitability calculations, analogous to carbonaceous materials, show that the process is not profitable economically in any case, Fig. 8. The cost per kmol of methane recovered is much higher than in case of carbonaceous materials. All the materials are above the limit to use the gas in a turbine, with zeolite 13X remarkably close to it. Zeolite 13X corresponds to the material with the lowest BET specific surface area, the lowest total pore volume and low CH_4/N_2 selectivity.

3.3. MOF materials

As noted in the literature, MOFs are the least used materials among the three considered, mainly due to their novelty, since they present really suitable properties related to adsorption processes. In this work, three different MOFs are studied: MIL-101(Cr), MOF-508 and Basolite C300. MIL-101(Cr) presents an ordered structure based on two sets of mesoporous cages that are accessible through microporous windows of 5.5 and 8.6 Å (Gómez et al., 2015), and Lewis acid sites, which give it remarkable stability towards water (Xu et al., 2009; Bakhtyari and Mofarahi, 2014; Kloutse et al., 2018). The three MOFs have shown resistance to mass transfer in micropores, the coefficients obtained being 0.027 s for MIL-101(Cr) (Liu et al., 2021), 0.46 s for MOF-508 (Bárcia et al., 2008), and 0.012 s for Basolite C300 (Ursueguía et al., 2020a), a commercial MOF homologous to the widely studied HKUST-1. Table 10 compiles the simulation parameters for the of the three MOF materials considered in the Aspen Adsorption software. Fig. 9A presents a comparison of the methane breakthrough curves obtained for the studied materials, both by TSA and PSA, whereas the total methane adsorption capacities in each case is shown in Fig. 9B.

The methane adsorption capacity of MOFs is similar to the case of carbonaceous materials. The methane adsorption capacity ratio (PSA/TSA) is 3.4, 3.02 and 3.03, respectively for MIL-101(Cr), MOF-508 and Basolite C300, demonstrating lower pressure influence than in case of carbonaceous materials, and similar to zeolites. As in the case of zeolites, pore size also greatly influences the adsorption process. On the other hand, Fig. 10 presents the methane concentration stage at the desorption stream by both techniques. MOF-508 is not able to reach the desired 1% of methane at the outlet, with a maximum concentration of 0.53%, which is, in fact, lower than the incoming methane, due to its large affinity towards nitrogen ($CH_4/N_2 = 1$). A maximum concentration of 2.6% is obtained in case of Basolite C300, which constitutes an enrichment of 78%, and 2% in case of MIL-101(Cr), an enrichment of 71.5%. Similarly to zeolitic materials, the maximum concentrations obtained

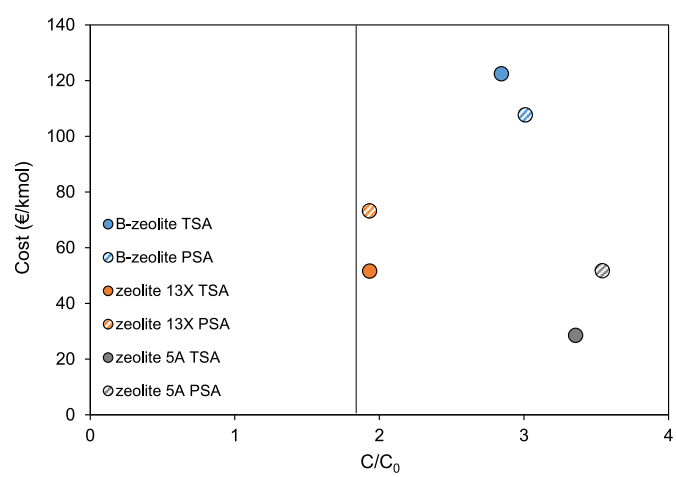

Fig. 8. Relation for all the zeolitic materials between cost per kmol of methane recovered and the concentration times from the initial methane concentration ($C_0 = 0.57\%$). Vertical black line points out the minimum concentration factor necessary to use the obtained stream as feed in a gas turbine (1% CH_4).

Table 9
Costs associated to the main stages in TSA and PSA processes (Couper et al., 2005).

Material	Adsorbent (k€)	Vessels (k€)	Heating[a] (k€)	Exchanger[a] (k€)	Pressurization[b] (k€)	Compressor[b] (k€)
β-zeolite	450.6	206.5	16.9	15.4	163.5	128.8
Zeolite 13X	299.5	206.5	12.5	15.2	319.7	128.8
Zeolite 5A	183.7	206.5	11.9	15.4	232.2	128.8

[a] Used in TSA processes.
[b] Used in PSA processes.

Table 10
Simulation parameters for TSA and PSA for the three MOF materials considered.

TSA (P = 1 bar)									
Material	$\dot{n}$ (mol/s)	L (m)	D (m)	ε_b	ρ_b (kg/m^3)	d_p (mm)	$1/K_L$ (s)	D_m (m^2/s) (ads/des)	T (K) (ads/des)
MIL-101(Cr)	60	10	2.5	0.4	390	1.5	0.027	$2.1\cdot10^{-5}/2.2\cdot10^{-5}$	288/313
MOF-508	60	10	2.5	0.74	430	4.6	0.46	$2.16\cdot10^{-5}/2.4\cdot10^{-5}$	303/323
Basolite C300	60	10	2.5	0.62	220	2	0.012	$2.1\cdot10^{-5}/2.4\cdot10^{-5}$	298/323
PSA (T = 288, 303 and 298 K, respectively for MIL-101, MOF-508 and Basolite C300)									
Material	$\dot{n}$ (mol/s)	L (m)	D (m)	ε_b	ρ_b (kg/m^3)	d_p (mm)	$1/K_L$ (s)	D_m (m^2/s) (ads/des)	P (bar) (ads/des)
MIL-101(Cr)	60	10	2.5	0.4	390	1.5	0.027	$7\cdot10^{-6}/2.1\cdot10^{-5}$	1/3
MOF-508	60	10	2.5	0.74	430	4.6	0.46	$7.2\cdot10^{-6}/2.16\cdot10^{-5}$	1/3
Basolite C300	60	10	2.5	0.62	220	2	0.012	$7\cdot10^{-6}/2.1\cdot10^{-5}$	1/3

are in case of PSA processes, but the difference between PSA and TSA is lower. The selectivities CH_4/N_2 are 2.2, 1 and 1.2, respectively for MIL-101(Cr), MOF-508 and Basolite C300. Basolite C300 demonstrates also large selectivity towards carbon dioxide, with a maximum concentration obtained of 2.7% CO_2. Table 11 indicates the total recovery of methane for each case at saturation conditions. The higher adsorption capacities in case of PSA processes lead to higher total methane recoveries. The high recovery of methane in case of MOF-508 is surprising, indicating that it is a material with a high adsorption capacity, but that sacrifices selectivity, without final increase in concentration.

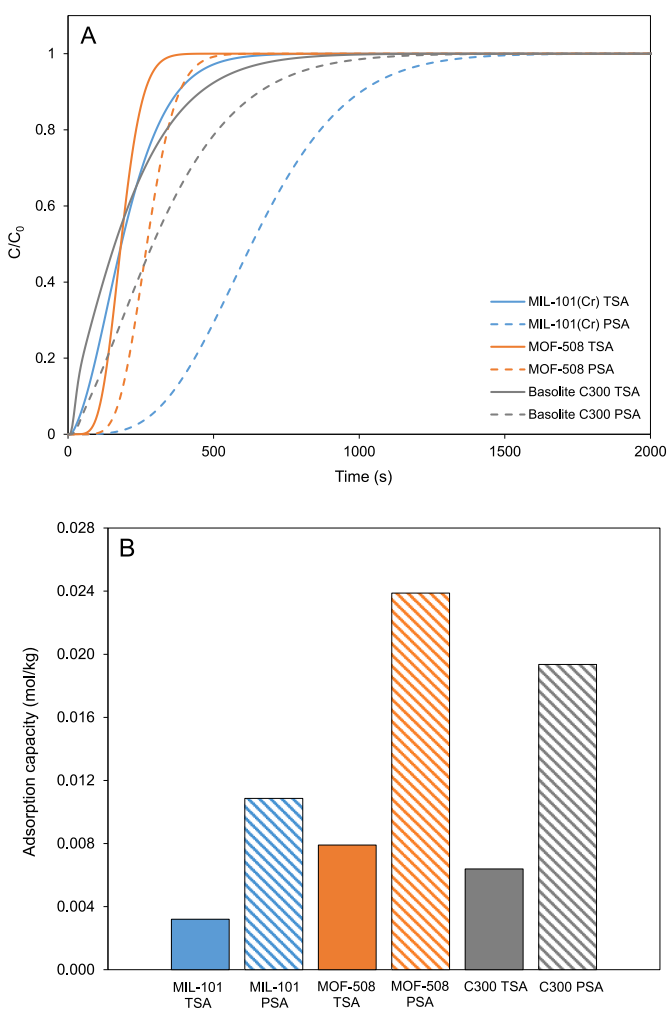

Fig. 9. Methane breakthrough curves (A) and methane adsorption capacity (B) for the MOFs considered. TSA processes were performed at 288 K for MIL-101, 303 K for MOF-508 and 298 K for Basolite C300, 1 bar, whereas PSA processes were performed at 288 K for MIL-101, 303 K for MOF-508 and 298 K for Basolite C300, 3 bar.

Table 12 exhibits the associated costs for each material and adsorption technique calculated analogous to the previous cases.

It is observed that the total cost per year is in all cases lower for TSA processes, with higher differences than in zeolitic and carbonaceous materials (around 85%). Economic profitability estimation reveals that the process is not profitable economically, as shown in Fig. 11. The cost per kmol of methane recovered is much higher than in case of carbonaceous materials and zeolites, mainly related to the high cost of adsorbents. As it can be observed, MOF-508 is below the limit to use the recovered stream as feed in a gas turbine (1% CH_4).

3.4. Key properties of adsorbents

Once all the combinations between adsorbent material and adsorption technique have been simulated for the same process, conclusions can be drawn about the key parameters. The adsorption capacity is one of the main parameters to be considered. It can be related to high specific surface areas, high pore volume or even the presence of preferential adsorption sites along the structure. In addition, the adsorption capacity

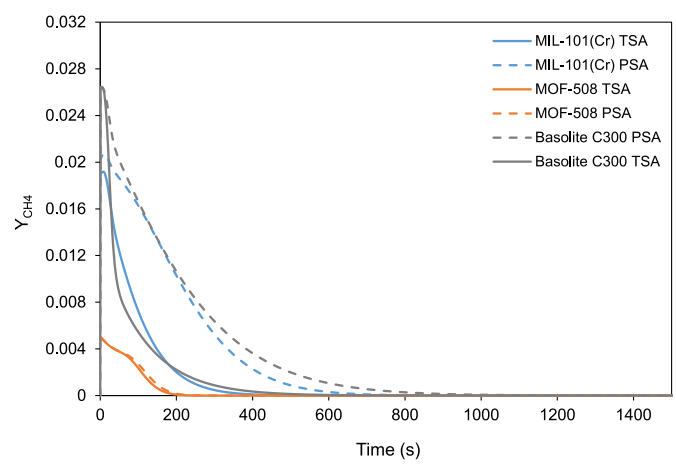

Fig. 10. Methane desorption curves for MIL-101(Cr) (blue), MOF-508 (orange) and Basolite C300 (grey). Continuous lines correspond to TSA processes, and discontinuous lines correspond to PSA processes.

Table 11
Methane recovery values for each process with MOFs.

Material	Process	CH_4 recovery (%)
MIL-101(Cr)	TSA	28.2
	PSA	44.4
MOF-508	TSA	99.8
	PSA	100
Basolite C300	TSA	21.6
	PSA	56.9

Table 12
Costs associated to the main stages in TSA and PSA processes (Couper et al., 2005).

Material	Adsorbent (k€)	Vessels (k€)	Heating[a] (k€)	Exchanger[a] (k€)	Pressurization[b] (k€)	Compressor[b] (k€)
MIL-101(Cr)	530.1	206.5	22.8	15.4	5918.2	128.8
MOF-508	470.9	206.5	8.04	13.1	4800.8	128.8
Basolite C300	265.6	206.5	21.3	15.2	2262.9	128.8

[a] Used in TSA processes.
[b] Used in PSA processes.

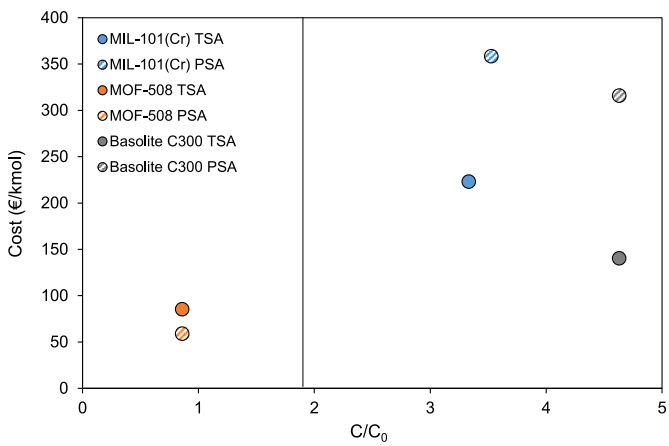

Fig. 11. Relation for all the MOF materials between cost per kmol of methane recovered and the concentration times from the initial methane concentration ($C_0 = 0.57\%$). Vertical black line points out the minimum concentration factor necessary to use the obtained stream as feed in a gas turbine (1% CH_4).

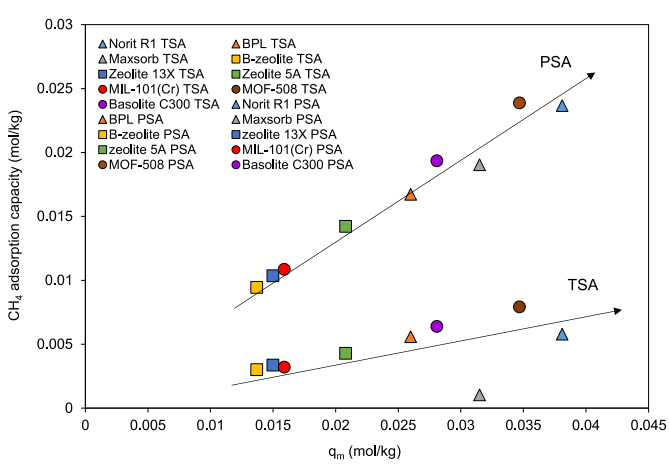

Fig. 12. Relationship between methane adsorption capacity and maximum capacity parameter (q_m) of Langmuir equation for TSA and PSA based on the different materials studied.

in each technique can be related to the parameters of the Langmuir isotherm (q_m and b) and to the mass transfer resistance ($1/K_L$). Fig. 12 plots the relationship between q_m and the adsorption capacity for both techniques, PSA and TSA, demonstrating an almost linear trend, with larger influence in case of PSA. Therefore, it is more convenient to use materials with high q_m values, obtaining better results in case of PSA. Other parameters, such as the resistance parameter, $1/K_L$, and the affinity parameter, b, which can be related to the adsorption enthalpy, show no clear influence on the methane adsorption capacity.

Further, the breakthrough curve shape and time are also important parameters: as it was deduced, the shape depends mainly on the adsorbate mass transfer across the adsorbent structure, whereas the breakthrough time is more related to the adsorption capacity. The highest diffusivities are associated to carbonaceous materials, with resistances based mainly in the micropore transport, which results in a more pronounced shape of the rupture curve at low times. Besides, there are also differences between PSA and TSA, the former with higher adsorption capacities, requires longer time to reach saturation. Although the adsorption capacity plays a key role in the methane recovery, it is remarkable that the best recovery values were obtained for zeolites and MOFs, highlighting the importance of the adsorbent densities, with more methane recovered for the same fixed bed volume. Concerning the concentration factor (C/C_0), it depends mainly on the CH_4/N_2 and CH_4/CO_2 selectivities of each material. An elevated selectivity towards methane increases the final concentration factor, especially in the case of activated carbons. It is also worth mentioning that the selectivity towards CO_2 is of interest to be as low as possible, to avoid possible impurity for later applications. This is a key point at which zeolites usually fail. Finally, the total cost associated to the process which depends directly on the material and the technique used. It was demonstrated that PSA processes are more expensive than TSA in all cases, as well as MOFs, with the highest costs per kmol of methane recovered, followed by zeolites, and activated carbons.

4. Conclusions and future perspectives

This work studied the diverse ways of harnessing VAM methane emissions generated in the shafts of the underground coal mining exploitations through fixed-bed adsorption. Two variable parameters have been considered: adsorbent material (Norit R1, BPL, Maxsorb, β-zeolite, zeolite 5A, zeolite 13X, Basolite C300, MIL-101(Cr) and MOF-508), and adsorption technique (TSA and PSA). After a design of the operation following the heuristic rules, all possible combinations were simulated, according to a rigorous mathematical model, by Aspen Adsorption software. Carbonaceous materials, especially Norit R1, obtained the highest concentrations in outlet streams, due to their high CH_4/N_2 selectivities. These materials also present the lowest methane recoveries (around 30%), mainly related to their low density, and the lowest costs per kmol of methane recovered. Desorption at maximum concentration spends a brief time in all the cases. In addition, MOFs, especially Basolite C300 and MOF-508, can retain a large amount of methane, due to the presence of open metal sites and high specific surface areas. The CH_4/N_2 selectivities are lower than in carbonaceous materials and, therefore, the final methane concentrations obtained are lower. The methane recoveries are really high in these materials, reaching even a 100% in case of MOF-508, but sacrificing certain selectivity towards methane. The costs per kmol of methane recovered are the highest among the materials studied, due mainly to the elevated cost associated to the synthesis of these new materials. Finally, zeolitic materials present the lowest final methane concentration obtained, with intermediate methane recoveries. The costs per kmol of methane recovered are high, due to the low methane adsorption capacity demonstrated and certain affinity to nitrogen and carbon dioxide. Concerning the adsorption technique, TSA has shown higher final methane concentrations in case of carbonaceous materials and some MOFs. On the other hand, PSA allows obtaining higher total methane adsorbed on all the materials, remarking the high dependence of adsorption on the applied pressure, especially on carbonaceous materials. Finally, the economic comparison shows that TSA is, in all cases, more convenient than PSA. Therefore, based on these

results, the most competitive combinations include TSA and materials with either high specific surface area or presence of open metal sites, high CH_4/N_2 and CH_4/CO_2 selectivity, high material density and with the lowest cost per kg as possible. In case of low selectivities or low material density, the application of PSA processes with good working capacities in the pressure working range, can improve the yield of the process.

Finally, concerning the limitations of the work, the most important is the applicability of the mathematical model. The assumptions made allow its application only to low concentration inlet methane streams, as the case of VAM emissions. Therefore, one of the ways of potential future research that opens is to improve and expand the mathematical model to be able to cover a wider range of conditions (CBM and AMM streams), for which a greater record of experimental results at higher concentrations of methane is needed and nowadays not available.

Credit author statement

David Ursueguía: Writing – original draft, Software, Data curation, Writing – review & editing, Formal analysis. Eva Díaz: Writing – review & editing, Visualization, Conceptualization, Project administration. Salvador Ordóñez: Visualization, Conceptualization, Project administration, Supervision.

Declaration of competing interest

The authors declare that they have no known competing financial interests or personal relationships that could have appeared to influence the work reported in this paper.

Data availability

Data will be made available on request.

Acknowledgments

This work was supported by the Research Fund of Coal and Steel of the European Union (contract RFCS216-754077-METHENERGY PLUS) and the Government of the Principality of Asturias (GRUPIN AYUD/2021/50450).David Ursueguía acknowledges the Spanish Ministry of Education for the PhD grant that supports his research: FPU2018-01448.

References

Al-Naddaf, Q., Thakkar, H., Rezaei, F., 2018; Novel. zeolite-5A@MOF-74 composite adsorbents with core-shell structure for H2 purification. ACS Appl. Mater. Interfaces 10, 29656–29666. https://doi.org/10.1021/acsami.8b10494, 2018.

Bae, J., Su, S., Yu, X., 2014. Enrichment of ventilation air Methane (VAM) with carbon fiber composites. Environ. Sci. Technol. 48, 6043–6049. https://doi.org/10.1021/es500025c, 2014.

Bae, J., Su, S., Yu, X., Yin, J., Villella, A., Jara, M., Loney, M., 2020. Site trials of ventilation air methane enrichment with two-stage vacuum, temperature, and vacuum swing adsorption. Ind. Eng. Chem. Res. 35, 15732–15741. https://doi.org/10.1021/acs.iecr.0c02616, 2020.

Bahamon, D., Vega, L., 2016. Systematic evaluation of materials for post-combustion CO_2 capture in a Temperature Swing Adsorption process. Chem. Eng. J. 284, 438–447. https://doi.org/10.1016/j.cej.2015.08.098, 2016.

Bakhtyari, A., Mofarahi, M., 2014. Pure and binary adsorption equilibria of methane and nitrogen on zeolite 5A. J. Chem. Eng. Data 59, 626–639. https://doi.org/10.1021/je4005036, 2014.

Bárcia, P., Bastin, L., Hurtado, E., Silva, J., Rodrigues, A., Chen, B., 2008. Single and multicomponent sorption of CO_2, CH_4 and N_2 in a microporous metal-organic framework. Separ. Sci. Technol. 43, 3494–3521. https://doi.org/10.1080/01496390802282347, 2008.

Bastin, L., Bárcia, P., Hurtado, E., Silva, J., Rodrigues, A., Chen, B., 2008. A microporous metal-organic framework for separation of CO_2/N_2 and CO_2/CH_4 by fixed-bed adsorption. J. Phys. Chem. C 112, 1575–1581. https://doi.org/10.1021/jp077618g, 2008.

Ben-Mansour, R., Qasem, N., 2018. An efficient temperature swing adsorption (TSA) process for separating CO_2 from CO_2/N_2 mixture using Mg-MOF-74. Energy Convers. Manag. 156, 10–24. https://doi.org/10.1016/j.enconman.2017.11.010, 2018.

Brandt, A., Heath, G., Kort, E., O'Sullivan, F., Pétron, G., Jordaan, S., Tans, P., Wilcox, J., Gopstein, A., Arent, D., Wofsy, S., Brown, N., Bradley, R., Stucky, G., Eardley, D., Harriss, R., 2014. Methane leaks from North American natural gas systems. Science 343, 733–735. https://doi.org/10.1126/science.1247045, 2014.

Brea, P., Delgado, J., Águeda, V., Uguina, M., 2017. Modeling of breakthrough curves of N_2, CH_4, CO, CO_2 and a SMR type off-gas mixture on a fixed bed of BPL activated carbon. Separ. Purif. Technol. 179, 61–71. https://doi.org/10.1016/j.seppur.2017.01.054, 2017.

Canevesi, R., Borba, C., Silva, E., Grande, C., 2019. Towards a design of a pressure swing adsorption unit for small scale biogas upgrading at. Energy Proc. 158, 848–853. https://doi.org/10.1016/j.egypro.2019.01.220, 2019.

Cavenati, S., Grande, C., Rodrigues, A., 2004. Adsorption equilibrium of methane, carbon dioxide, and nitrogen on zeolite 13X at high pressures. J. Chem. Eng. Data 49, 1095–1101. https://doi.org/10.1021/je0498917, 2004.

Cavenati, S., Grande, C., Rodrigues, A., 2006. 2006; Separation of CH4/CO2/N2 mixtures by layer$_e$d p$_r$es$_s$ure swing adsorption for upgrade of natural gas. Chem. Eng. Sci. 61, 3893–3906. https://doi.org/10.1016/j.ces.2006.01.023.

Chaemwinyoo, U., Marín, P., Martín, C.F., Díez, F.V., Ordóñez, S., 2022. Assessment of an integrated adsorption-regenerative catalytic oxidation process for the harnessing of lean methane emissions. J. Environ. Chem. Eng. 10, 107013 https://doi.org/10.1016/j.jece.2021.107013, 2022.

Chen, L., Deng, S., Zhao, R., Zhu, Y., Zhao, L., Li, S., 2021. Temperature swing adsorption for CO2 capture: thermal design and management on adsorption bed with single-tube/three-tube internal heat exchanger. Appl. Therm. Eng. 199, 117538 https://doi.org/10.1016/j.applthermaleng.2021.117538, 2021.

Cheng, W., Nie, W., Yu, H., Zheng, A., 2017. Development Status of Dust-Control Technologies for the Mechanized Mining Working Face in China, NexGen Technologies for Mining and Fuel Industries. Allied Publishers PVT.

Climate and energy framework. Greenhouse gas emissions – raising the ambition, 2020. https://ec.europa.eu/clima/policies/strategies/2030_en. (Accessed 6 June 2021).

Costs Reports and Guidance for Air Pollution Regulations, 2018. https://www.epa.gov/economic-and-cost-analysis-air-pollution-regulations/cost-reports-and-guidance-air-pollution. (Accessed 20 May 2021).

Couper, J., Penney, W., Fair, J., Walas, S., 2005. Chemical Process Equipment: Selection and Design, third ed. Elsevier, Waltham (MA).

Damassa, T., 2014. Climate Analysis Indicators Tool (CAIT), Encyclopedia of Quality of Life and Well-Being Research. https://doi.org/10.1007/978-94-007-0753-5_403, 2014.

Dantas, T., Luna, F., Silva, I., Azevedo, D., Grande, C., Rodrigues, A., Moreira, R., 2011. Carbon dioxide-nitrogen separation through adsorption on activated carbon in a fixed bed. Chem. Eng. J. 169, 11–19. https://doi.org/10.1016/j.cej.2010.08.026, 2011.

Delgado, J., Águeda, V., Uguina, M., Sotelo, J., Brea, P., Grande, C., 2014. Adsorption and diffusion of H_2, CO, CH_4, and CO_2 in BPL activated carbon and 13X zeolite: evaluation of performance in pressure swing adsorption hydrogen purification by simulation. Ind. Eng. Chem. Res. 53, 15414–15426. https://doi.org/10.1021/ie403744u, 2014.

Denysenko, A., Evans, M., Kholod, N., Butler, N., Roshchanka, V., 2018. Legal and Regulatory Status of Abandoned Mine Methane in Selected Countries: Considerations for Decision Makers. Pacific Northwest National Laboratory. https://doi.org/10.13140/RG.2.2.21171.89124, 2018.

Dreisbach, F., Staudt, R., Keller, J., 1999. High pressure adsorption data of methane, nitrogen, carbon dioxide and their binary and ternary mixtures on activated carbon. Adsorption 5, 215–227. https://doi.org/10.1023/A:1008914703884, 1999.

Du, J., Wang, Q., Wang, Y., Guo, Y., Li, R., 2019. A hierarchical zeolite Beta with well-connected pores via using graphene oxide. Mater. Lett. 250, 139–142. https://doi.org/10.1016/j.matlet.2019.05.014, 2019.

Duda, A., Krzemien, A., 2018. Forecast of methane emission from closed underground coal mines exploited by longwall mining – a case study of Anna coal mine. J. Sust. Mining. 17, 184–194. https://doi.org/10.1016/j.jsm.2018.06.004, 2018.

Equipment costs, 2003. Plant Design and Economics for Chemical Engineers. https://www.mhhe.com/engcs/chemical/peters/data/. (Accessed 25 May 2021). accessed.

Gabelman, A., 2017. Adsorption Basics: Part 1. https://www.aiche.org/resources/publications/cep/23017/july/adsorption-basics-part-1. (Accessed 15 May 2020). Accessed.

Gao, W., Yan, W., Cai, R., Williams, K., Salas, A., Wojtas, L., Shi, X., Ma, S., 2012. A pillared metal-organic framework incorporated with 1,2,3-triazole moieties exhibiting remarkable enhancement of CO_2 uptake. Chem. Commun. 48, 8898–8900. https://doi.org/10.1039/C2CC34380K, 2012.

Ghazvini, M., Vahedi, M., Nobar, S., Sabouri, F., 2021. Investigation of the MOF adsorbents and the gas adsorptive separation mechanisms. J. Environ. Chem. Eng. 9, 104790 https://doi.org/10.1016/j.jece.2020.104790, 2021.

Gholipour, F., Mofarahi, M., 2016. Adsorption equilibrium of methane and carbon dioxide on zeolite 13X: experimental and thermodynamic modeling. J. Supercrit. Fluids 111, 47–54. https://doi.org/10.1016/j.supflu.2016.01.008, 2016.

Ghoshal, A., Manjare, S., 2002. Selection of appropriate adsorption technique for recovery of VOCs: an analysis. J. Loss Prev. Process. Ind. 15, 413–421. https://doi.org/10.1016/S0950-4230(02)00042-6, 2002.

Golden, T., Kumar, R., 1993. Adsorption equilibrium and kinetics for multiple trace impurities in various gas streams on activated carbon. Ind. Eng. Chem. Res. 32, 159–165. https://doi.org/10.1021/ie00013a021, 1993.

Gómez, L., Zacharia, R., Bénard, P., Chahine, R., 2015. Multicomponent adsorption of biogas compositions containing CO_2, CH_4 and N_2 on Maxsorb and Cu-BTC using extended Langmuir and Doong-Yang models. Adsorption 21, 433–443. https://doi.org/10.1007/s10450-015-9684-6, 2015.

Han, M., Li, X., Lin, S., 2002. Diffusion transfer in the course of benzene alkylation with propylene over a β-zeolite catalyst. Theor. Found. Chem. Eng. 36, 259–263. https://doi.org/10.1023/A:1015847904709, 2002.
Hartmann, M., Fischer, M., 2012. Amino-functionalized basic catalysts with MIL-101 structure. Microporous Mesoporous Mater. 164, 38–43. https://doi.org/10.1016/j.micromeso.2012.06.044, 2012.
Himeno, S., Komatsu, T., Fujita, S., 2005. High-pressure adsorption equilibria of methane and carbon dioxide on several activated carbons. J. Chem. Eng. Data 50, 369–376. https://doi.org/10.1021/je049786x, 2005.
Howarth, R., 2014. A bridge to nowhere: methane emissions and the greenhouse gas footprint of natural gas. Energy Sci. Eng. 2, 47–60. https://doi.org/10.1002/ese3.35, 2014.
Jadhav, P., Chatti, R., Biniwale, R., Labhsetwar, N., Devotta, S., Rayalu, S., 2007. Monoethanol amine modified zeolite 13X for CO_2 adsorption at different temperatures. Energy Fuel. 21, 3555–3559. https://doi.org/10.1021/ef070038y, 2007.
Jensen, N., Rufford, T., Watson, G., Zhang, D., Chan, K., May, E., 2012. Screening zeolites for gas separation applications involving methane, nitrogen, and carbon dioxide. J. Chem. Eng. Data 57, 106–113. https://doi.org/10.1021/je200817w, 2012.
Ju, Y., Sun, Y., Sa, Z., Pan, J., Wang, J., Hou, Q., Li, Q., Yan, Z., Liu, J., 2016. A new approach to estimate fugitive methane emissions from coal mining in China. Sci. Total Environ. 543A, 514–523. https://doi.org/10.1016/j.scitotenv.2015.11.024, 2016.
Karacan, C., Ruiz, F., Cotè, M., Phipps, S., 2011. Coal mine methane: a review of capture and utilization practices with benefits to mining safety and to greenhouse gas reduction. Int. J. Coal Geol. 86, 121–156. https://doi.org/10.1016/j.coal.2011.02.009, 2011.
Karimi, K., Fatemi, S., 2021. Methane capture and nitrogen purification from a nitrogen rich reservoir by pressure swing adsorption; experimental and simulation study. J. Environ. Chem. Eng. 9, 106210 https://doi.org/10.1016/j.jece.2021.106210, 2021.
Khokhar, N., Park, J., 2017. A simplified sampling procedure for the estimation of methane emission in rice fields. Environ. Monit. Assess. 189, 468. https://doi.org/10.1007/s10661-017-6184-z, 2017.
Kholod, N., Evans, M., Pilcher, R., Roshchanka, V., Ruiz, F., Coté, M., Collings, R., 2020. Global methane emissions from coal mining to continue growing even with declining coal production. J. Clean. Prod. 256, 120489 https://doi.org/10.1016/j.jclepro.2020.120489, 2020.
Kilkis, S., Krajacic, G., Duic, N., Rosen, M., Al-Nimr, M., 2020. Advances in integration of energy, water, and environment systems towards climate neutrality for sustainable development. Energy Convers. Manag. 225, 113410 https://doi.org/10.1016/j.enconman.2020.113410, 2020.
Kim, Y., Nam, Y., Kang, Y., 2015. Study on a numerical model and PSA (pressure swing adsorption) process experiment for CH_4/CO_2 separation from biogas. Energy 91, 732–741. https://doi.org/10.1016/j.energy.2015.08.086, 2015.
Klein, L., Ramachandran, M., Kessel, T., Nair, D., Hinds, N., Hamann, H., Sosa, N., 2018. Wireless Sensor Networks for Fugitive Methane Emissions Monitoring in Oil and Gas Industry. IEEE International Congress on Internet of Things (ICIOT), pp. 41–48. https://doi.org/10.1109/ICIOT.2018.00013, 2018.
Kloutse, F., Hourri, A., Natarajan, S., Benard, P., Chahine, R., 2018. Hydrogen separation by adsorption: experiments and modelling of H_2-N_2-CO_2 and H_2-CH_4-CO_2 mixtures adsorption on CuBTC and MOF-5. Microporous Mesoporous Mater. 271, 175–185. https://doi.org/10.1016/j.micromeso.2018.05.042, 2018.
Kumar, S., 2018. Mineral Exploration: Principles and Applications, second ed. https://doi.org/10.1016/C2017-0-00902-3
Li, P., Tezel, H., 2007. Adsorption separation of N_2, O_2, CO_2 and CH_4 gases by β-zeolite. Microporous Mesoporous Mater. 98, 94–101. https://doi.org/10.1016/j.micromeso.2006.08.016, 2007.
Li, Y.L., Liu, Y.S., Yang, X., 2013. Proportion pressure swing adsorption for low concentration coal mine methane. Enrichment 48 (8), 1201–1210. https://doi.org/10.1080/01496395.2012.732979, 2013.
Liu, Z., Grande, C., Li, P., Yu, J., Rodrigues, A., 2011. Adsorption and desorption of carbon dioxide and nitrogen on zeolite 5A. Separ. Sci. Technol. 46, 434–451. https://doi.org/10.1080/01496395.2010.513360, 2011.
Liu, J., Cao, H., Shi, Y., Jiang, P., 2021. Enhanced methane delivery in MIL-101(Cr) by means of subambient cooling. Energy Fuel. 35 (2021), 6898–6908. https://doi.org/10.1021/acs.energyfuels.1c00617.
Luberti, M., Ahn, H., 2022. Review of Polybed pressure swing adsorption for hydrogen purification. Int. J. Hydrogen Energy 47 (2022), 10911–10933. https://doi.org/10.1016/j.ijhydene.2022.01.147.
Maring, B., Webley, P., 2013. A new simplified pressure/vacuum swing adsorption model for rapid adsorbent screening for CO_2 capture applications. Int. J. Greenh. Gas Control 15, 16–31. https://doi.org/10.1016/j.ijggc.2013.01.009, 2013.
McEwen, J., Hayman, J., Yazaydin, A., 2013. A comparative study of CO_2, CH_4 and N_2 adsorption in ZIF-8, zeolite-13X and BPL activated carbon. Chem. Phys. 412, 72–76. https://doi.org/10.1016/j.chemphys.2012.12.012, 2013.
Munusamy, K., Sethia, G., Patil, D., Rallapalli, P., Somani, R., Bajaj, H., 2012. Sorption of carbon dioxide, methane, nitrogen and carbon monoxide on MIL-101(Cr): volumetric measurements and dynamic adsorption studies. Chem. Eng. J. 195–196, 359–368. https://doi.org/10.1016/j.cej.2012.04.071, 2012.
Neves, M., Gkaniatsou, E., Nouar, F., Pinto, M., Serre, C., 2021. MOF Industrialization: a Complete Assessment of Production Costs. Faraday Discussions. https://doi.org/10.1039/D1FD00018G, 2024.
NIST's Standard Reference Database Number 69. https://doi.org/10.18434/T4D303.
Niu, Z., Cui, X., Pham, T., Lan, P., Xing, H., Forrest, K., Wojtas, L., Space, B., Ma, S., 2019. A metal-organic framework based methane nano-trap for the capture of coal-mine methane. Angew. Chem. Int. Ed. 58, 10138–10141. https://doi.org/10.1002/anie.201904507, 2019.
Nobar, S., Farooq, S., 2012. Experimental and modeling study of adsorption and diffusion of gases in Cu-BTC. Chem. Eng. Sci. 84, 801–813. https://doi.org/10.1016/j.ces.2012.05.022, 2012.
Ortiz, F., Barragán, M., Yang, R., 2019. Modeling of fixed-bed columns for gas physical adsorption. Chem. Eng. J. 378, 121985 https://doi.org/10.1016/j.cej.2019.121985, 2019.
Ouyang, S., Xu, S., Song, N., Jiao, S., 2013. Coconut shell-based carbon adsorbents for ventilation air methane enrichment. Fuel 113, 420–425. https://doi.org/10.1016/j.fuel.2013.06.004, 2013.
Pandey, R., Harpalani, S., 2019. Evaluation of Dynamic Flow and Production Behavior of Biogenic Methane Reservoirs. In: 53rd U.S. Rock Mechanics/Geomechanics Symposium. New York City, New York, 2019.
Park, S., Liang, Y., 2016. Biogenic methane production from coal: a review on recent research and development on microbially enhanced coalbed methane (MECBM). Fuel 166, 258–267. https://doi.org/10.1016/j.fuel.2015.10.121, 2016.
Peredo-Mancilla, D., Ghimbeu, C., Ho, B., Jeguirim, M., Hort, C., Bessieres, D., 2019. Comparative study of the CH_4/CO_2 adsorption selectivity of activated carbons for biogas upgrading. J. Environ. Chem. Eng. 7, 103368 https://doi.org/10.1016/j.jece.2019.103368, 2019.
Perego, C., Peratello, S., 1999. Experimental methods in catalytic kinetics. Catal. Today 52, 133–145. https://doi.org/10.1016/S0920-5861(99)00071-1, 1999.
Perry, R., Green, D., 1997. Perry's Chemical Engineer's Handbook, seventh ed. McGraw-Hill. 1997. Section 11.
Pieprzyk, B., Hilje, P., 2018. Influence of methane emissions on the GHG emissions of fossil fuels. Biofuels, Bioproducts and Biorefining 13, 535–551. https://doi.org/10.1002/bbb.1959, 2018.
Qadir, S., Li, D., Gu, Y., Yuan, Z., Zhao, Y., Wang, S., Wang, S., 2021. Experimental and numerical investigations on the separation performance of $[Cu(INA)_2]$ adsorbent for CH_4 recovery by VPSA from oxygen-bearing coal mine methane. Chem. Eng. J. 408, 127238 https://doi.org/10.1016/j.cej.2020.127238, 2021.
Qu, D., Yang, Y., Qian, Z., Li, P., Yu, J., Ribeiro, A., Rodrigues, A., 2020. Enrichment of low-grade methane gas from nitrogen mixture by VPSA with CO_2 displacement process: modeling and experiment. Chem. Eng. J. 380, 122509 https://doi.org/10.1016/j.cej.2019.122509, 2020.
Querejeta, N., García, S., Álvarez-Gutiérrez, N., Rubiera, F., Pevida, C., 2019. Measuring heat capacity of activated carbons for CO_2 capture. J. CO2 Util. 33, 148–156. https://doi.org/10.1016/j.jcou.2019.05.018, 2019.
Rainone, F., D'Agostino, O., Erto, A., Balsamo, M., Lancia, A., 2021. Biogas upgrading by adsorption onto activated carbon and carbon molecular sieves: experimental and modelling study in binary CO_2/CH_4 mixture. J. Environ. Chem. Eng. 9, 106256 https://doi.org/10.1016/j.jece.2021.106256.
Rupa, M., Pal, A., Mitra, S., Saha, B., 2021. Time adapted linear driving force model for gas adsorption onto solids. Chem. Eng. J. 420, 129785 https://doi.org/10.1016/j.cej.2021.129785, 2021.
Ryckebosch, E., Drouillon, M., Vervaeren, H., 2011. Techniques for transformation of biogas to biomethane. Biomass Bioenergy 35, 1633–1645. https://doi.org/10.1016/j.biombioe.2011.02.033, 2011.
Sabouni, R., Kazemian, H., Rohani, S., 2013. Mathematical modeling and experimental breakthrough curves of carbon dioxide adsorption on metal organic framework CPM-5. Environ. Sci. Technol. 47, 9372–9380. https://doi.org/10.1021/es401276r, 2013.
Sapart, C., Monteil, G., Prokopiou, M., van de Wal, R., Kaplan, J., Sperlich, P., Krumhardt, K., van der Veen, C., Houweling, S., Krol, M., Blunier, T., Sowers, T., Martinerie, P., Witrant, E., Jensen, D., Röckmann, T., 2012. Natural and anthropogenic variations in methane sources during the past two millennia. Nature 490, 85–88. https://doi.org/10.1038/nature11461, 2012.
Schoell, M., 1988. Multiple origins of methane in the Earth. Chem. Geol. 71, 1–10. https://doi.org/10.1016/0009-2541(88)90101-5, 1998.
Schoenecker, P., Carson, C., Jasuja, H., Flemming, C., Walton, K., 2012. Effect of water adsorption on retention of structure and surface area of metal-organic frameworks. Ind. Eng. Chem. Res. 51, 6513–6519. https://doi.org/10.1021/ie202325p, 2012.
Sheikh, M., Hassan, M., Loughlin, K., 1996. Adsorption equilibria and rate parameters for nitrogen and methane on Maxsorb activated carbon. Gas Separ. Purif. 10, 161–168. https://doi.org/10.1016/0950-4214(96)00017-5, 1996.
Silva, J., Ferreira, A., Mendes, P., Cunha, A., Gleichmann, K., Rodrigues, A., 2015. Adsorption equilibrium and dynamics of fixed bed adsorption of CH_4/N_2 in binderless beads of 5A zeolite. Ind. Eng. Chem. Res. 54, 6390–6399. https://doi.org/10.1021/acs.iecr.5b01608, 2015.
Silvestre-Albero, J., Salazar, C., Sepúlveda-Escribano, A., Rodríguez-Reinoso, F., 2001. Characterization of Microporous solids by immersion calorimetry. Colloids Surf. A Physicochem. Eng. Asp. 187–188, 151–165. https://doi.org/10.1016/S0927-7757(01)00620-3, 2001.
Sircar, S., Golden, T., Rao, M., 1996. Activated carbon for gas separation and storage. Carbon 34, 1–12. https://doi.org/10.1016/0008-6223(95)00128-X, 1996.
Su, S., Agnew, J., 2006. Catalytic combustion of coal mine ventilation air methane. Fuel 85, 1201–1210. https://doi.org/10.1016/j.fuel.2005.11.010, 2006.
Teo, H., Chakraborty, A., Kayal, S., 2017. Evaluation of CH_4 and CO_2 adsorption on HKUST-1 and MIL-101(Cr) MOFs employing Monte Carlo simulation and comparison with experimental data. Appl. Therm. Eng. 110, 891–900. https://doi.org/10.1016/j.applthermaleng.2016.08.126, 2017.
Thiagarajan, N., Kitchen, N., Xie, H., Ponton, C., Lawson, M., Formolo, M., Eiler, J., 2020. Identifying thermogenic and microbial methane in deep water Gulf of Mexico Reservoirs. Geochem. Cosmochim. Acta 275, 188–208. https://doi.org/10.1016/j.gca.2020.02.016, 2020.

UNECE, 2019. Best Practice Guidance for Effective Methane Recovery and Use from Abandoned Coal Mines. https://unece.org/fileadmin/DAM/energy/images/CMM/CMM_CE/AMM_BPG_FINAL.pdf. (Accessed 5 June 2021). accessed.

Ursueguía, D., Díaz, E., Vega, A., Ordóñez, S., 2020a. Methane separation from diluted mixtures by fixed bed adsorption using MOFs: model validation and parametric studies. Separ. Purif. Technol. 251, 117374 https://doi.org/10.1016/j.seppur.2020.117374, 2020.

Ursueguía, D., Díaz, E., Ordóñez, S., 2020b. Densification-induced structure changes in Basolite MOFs: effect on low-pressure CH_4 adsorption. Nanomaterials 10, 1089. https://doi.org/10.3390/nano10061089, 2020.

Ursueguía, D., Marín, P., Díaz, E., Ordóñez, S., 2021a. A new strategy for upgrading ventilation air methane emissions combining adsorption and combustion in a lean-gas turbine. J. Nat. Gas Sci. Eng. 88, 103808 https://doi.org/10.1016/j.jngse.2021.103808, 2021.

Ursueguía, D., Díaz, E., Ordóñez, S., 2021b. Metal-organic frameworks (MOFs) as methane adsorbents: from storage to diluted coal mining streams concentration. Sci. Total Environ. 790, 148211 https://doi.org/10.1016/j.scitotenv.2021.148211, 2021.

Vilardi, G., Bassano, C., Deiana, P., Verdone, N., 2020. Exergy and energy analysis of biogas upgrading by pressure swing adsorption: dynamic analysis of the process. Energy Convers. Manag. 226, 113482 https://doi.org/10.1016/j.enconman.2020.113482, 2020.

Vogtenhuber, H., Hofmann, R., Helminger, F., Schöny, G., 2018. Process simulation of an efficient temperature swing adsorption concept for biogas upgrading. Energy 162, 200–209. https://doi.org/10.1016/j.energy.2018.07.193, 2018.

Wang, X., Zhou, F., Ling, Y., Xiao, Y., Ma, B., Ma, X., Yu, S., Liu, H., Wei, K., Kang, J., 2021. Overview and outlook on utilization technologies of low-concentration coal mine methane. Energy Fuel. 35 (2021), 15398–15423. https://doi.org/10.1021/acs.energyfuels.1c02312.

Warmuzinski, K., 2008. Harnessing methane emissions from coal mining. Process Saf. Environ. Protect. 86, 315–320. https://doi.org/10.1016/j.psep.2008.04.003, 2008.

Wilkins, N., Rajendran, A., Farooq, S., 2020. Dynamic column breakthrough experiments for measurement of adsorption equilibrium and kinetics. Adsorption 27 (2020), 397–422. https://doi.org/10.1007/s10450-020-00269-6.

Wu, J., Claesson, O., Fangmark, I., Hammarstrom, L., 2005. A systematic investigation of the overall rate coefficient in the Wheeler-Jonas equation for adsorption on dry activated carbons. Carbon 43, 481–490. https://doi.org/10.1016/j.carbon.2004.09.024, 2005.

Xiu, G., Li, P., 2000. Prediction of breakthrough curves for adsorption of lead(II) on activated carbon fibers in a fixed bed. Carbon 38, 975–981. https://doi.org/10.1016/S0008-6223(99)00206-7, 2000.

Xu, X., Zhao, X., Sun, L., Liu, X., 2009. Adsorption separation of carbon dioxide, methane and nitrogen on monoethanol amine modified β-zeolite. J. Nat. Gas Chem. 18, 167–172. https://doi.org/10.1016/S1003-9953(08)60098-5, 2009.

Xu, H., Tang, D., Zhao, J., Li, S., Tao, S., 2015. A new laboratory method for accurate measurement of the methane diffusion coefficient and its influencing factors in the coal matrix. Fuel 158, 239–247. https://doi.org/10.1016/j.fuel.2015.05.046, 2015.

Xu, M., Wu, H., Lin, Y., Deng, S., 2018. Simulation and optimization of Pressure swing adsorption process for high-temperature air separation by perovskite sorbents. Chem. Eng. J. 354, 62–74. https://doi.org/10.1016/j.cej.2018.07.080, 2018.

Yang, R., 2003. Adsorbents: Fundamentals and Applications, first ed. John Wiley & Sons.

Yang, X., Liu, Y., Li, Z., Zhang, C., Xing, Y., 2018. Vacuum exhaust process in pilot-scale vacuum pressure swing adsorption for coal mine ventilation air methane enrichment. Energies 11, 1030. https://doi.org/10.3390/en11051030, 2018.

Yang, J., Bai, H., Shang, H., Wang, J., Li, J., Deng, S., 2020. Experimental and simulation study on efficient CH_4/N_2 separation by pressure swing adsorption on silicalite-1 pellets. Chem. Eng. J. 388, 124222 https://doi.org/10.1016/j.cej.2020.124222, 2020.

Yang, Z., Hussain, M.Z., Marín, P., Jia, Q., Wang, N., Ordóñez, S., Zhu, Y., Xia, Y., 2022. Enrichment of low concentration methane: an overview of ventilation air methane. J. Mater. Chem. 10 (2022), 6397–6413. https://doi.org/10.1039/d1ta08804a.

Yavary, M., Ebrahim, H., Falamaki, C., 2015. The effect of number of pressure equalization steps on the performance of pressure swing adsorption process. Chem. Eng. Process: Process Intensif. 87, 35–44. https://doi.org/10.1016/j.cep.2014.11.003, 20215.

Zheng, Y., Li, Q., Yuan, C., Tao, Q., Xhao, Y., Zhang, G., Liu, J., 2019. Influence of temperature on adsorption selectivity: coal-based activated carbon for CH_4 enrichment from coal mine methane. Powder Technol. 347, 42–49. https://doi.org/10.1016/j.powtec.2019.02.042, 2019.

Zhu, L., Shen, D., Luo, K., 2020. A critical review on VOCs adsorption by different porous materials: species, mechanisms and modification methods. J. Hazard Mater. 389, 122102 https://doi.org/10.1016/j.jhazmat.2020.122102, 2020.